water

MDPI

Article

Multi-Scale Variation in Surface Water Area in the Yellow River Basin (1991–2023) Based on Suspended Particulate Matter Concentration and Water Indexes

Zhiqiang Zhang [1,2], Xinyu Guo [1], Lianhai Cao [1,*], Xizhi Lv [3], Xiuyu Zhang [4], Li Yang [1], Hui Zhang [1], Xu Xi [5,*] and Yichen Fang [1]

1 College of Surveying and Geo-Informatics, North China University of Water Resources and Electric Power, Zhengzhou 450001, China; zhangzhiqiang@ncwu.edu.cn (Z.Z.); 201904419@stu.ncwu.edu.cn (X.G.); zhyl@ncwu.edu.cn (L.Y.); huihui945726@163.com (H.Z.); fangyichenncwu@163.com (Y.F.)
2 Key Laboratory of Geospatial Technology for Middle and Lower Yellow River Regions (Henan University), Ministry of Education, Kaifeng 475000, China
3 Yellow River Institute of Hydraulic Research, Zhengzhou 450003, China; nihulvxizhi@163.com
4 College of Water Resources, North China University of Water Resources and Electric Power, Zhengzhou 450001, China; zhangxiuyu@ncwu.edu.cn
5 School of Geography Science and Geomatics Engineering, Suzhou University of Science and Technology, Suzhou 215009, China
* Correspondence: caolianhai1970@163.com (L.C.); xixu@mail.usts.edu.cn (X.X.)

Abstract: Surface water is a crucial part of terrestrial ecosystems and is crucial to maintaining ecosystem health, ensuring social stability, and promoting high-quality regional economic development. The surface water in the Yellow River Basin (YRB) has a high sediment content and spatially heterogeneous sediment distribution, presenting a significant challenge for surface water extraction. In this study, we first analyze the applicability of nine water indexes in the YRB by using the Landsat series images (Landsat 5, 7, 8) and then examine the correlation between the accuracy of the water indexes and suspended particulate matter (SPM) concentrations. On this basis, we propose a surface water extraction method considering the SPM concentrations (SWE-CSPM). Finally, we examine the dynamic variations in the surface water in the YRB at four scales: the global scale, the secondary water resource zoning scale, the provincial scale, and the typical water scale. The results indicate that (1) among the nine water indexes, the MBWI has the highest water extraction accuracy, followed by the AWEInsh and WI2021, while the NDWI has the lowest. (2) Compared with the nine water indexes and the multi-index water extraction rule method (MIWER), the SWE-CSPM can effectively reduce the commission errors of surface water extraction, and the water extraction accuracy is the highest (overall accuracy 95.44%, kappa coefficient 90.62%). (3) At the global scale, the maximum water area of the YRB shows a decreasing trend, but the change amount is small. The permanent water area shows an uptrend, whereas the seasonal water area shows a downtrend year by year. The reason may be that the increase in surface runoff and the construction of reservoir projects have led to the transformation of some seasonal water into permanent water. (4) At the secondary water resource zoning scale, the permanent water area of other secondary water resource zonings shows an increasing trend in different degrees, except for the Interior Drainage Area. (5) At the provincial scale, the permanent water area of all provinces shows an uptrend, while the seasonal water areas show a fluctuating downtrend. The maximum water area of Shandong, Inner Mongolia Autonomous Region, and Qinghai increases slowly, while the other provinces show a decreasing trend. (6) At the typical water scale, there are significant differences in the water area variation process in Zhaling Lake, Eling Lake, Wuliangsuhai, Hongjiannao, and Dongping Lake, but the permanent water area and maximum water area of these waters have increased over the past decade. This study offers significant technical support for the dynamic monitoring of surface water and helps to deeply understand the spatiotemporal variations in surface water in the YRB.

Keywords: surface water extraction; surface water spatiotemporal variation; Yellow River Basin; suspended particulate matter

Citation: Zhang, Z.; Guo, X.; Cao, L.; Lv, X.; Zhang, X.; Yang, L.; Zhang, H.; Xi, X.; Fang, Y. Multi-Scale Variation in Surface Water Area in the Yellow River Basin (1991–2023) Based on Suspended Particulate Matter Concentration and Water Indexes. *Water* **2024**, *16*, 2704. https://doi.org/10.3390/w16182704

Academic Editor: Stefano Polesello

Received: 26 August 2024
Revised: 20 September 2024
Accepted: 20 September 2024
Published: 23 September 2024

1. Introduction

Surface water serves as a critical component of terrestrial ecosystems, which is essential for maintaining ecosystem health, ensuring social stability, and promoting high-quality regional economic development. The spatial pattern of global surface water has undergone significant changes primarily due to climate change and human activities' impact [1]. Previous studies have indicated that the global permanent water area has decreased by 90,000 km^2 over the past few decades, with over 70% of this loss concentrated in the Middle East and Asia [2]. Due to dam construction and water conservation policies, China's surface water area has increased by 9110 km^2 from 2000 to 2015 [3–5]. This indicates that although global water areas are generally decreasing, different regions exhibit varying trends. Extreme changes in surface water area often lead to severe water resource issues (such as floods, droughts, etc.), constrain regional economic development, and endanger people's lives and property safety [6]. Therefore, regional monitoring of surface water area changes is essential to mitigate the risks posed by extreme water issues.

Multi-spectral satellite remote sensing images have the advantages of large scale, low cost, and repeated observation, providing valuable data sources for the dynamic monitoring of surface water [7,8]. Compared to traditional site monitoring, remote sensing technology is more conducive to continuous surface water monitoring from a spatial perspective [6]. The water index method is widely used in surface water extraction based on remote sensing images [9]. The method is based on the principle that with the increase in the wavelength, water reflectance gradually decreases, with a higher reflectance observed in the blue-green band and lower reflectance in the infrared band. The Normalized Difference Water Index (NDWI) serves as the first water index leveraging the normalized difference between the green and near-infrared bands [10]. Numerous studies indicate that the NDWI has a good effect on water extraction in areas with high vegetation coverage but performs poorly in complex urban scenes [11]. To address the challenges, Xu [12] modified the NDWI by replacing the near-infrared band with the mid-infrared band. Water exhibits a lower reflectance in the mid-infrared and shortwave infrared bands, which is more effective than using the near-infrared band and shortwave infrared bands in the area covered with urban scenes. Previous studies have explored the applicability of the MNDWI in non-urban scenarios, and the results show that the MNDWI can easily misidentify snow, ice, and mountain shadows as surface water. Yan et al. [13] introduce a water–background linear mixed simulation based on the MNDWI for arid areas with sand, bare soil, and vegetated inland river. They propose the enhanced water index (EWI) to solve the problem of water extraction in arid river areas. To tackle shadow interference, Feyisa et al. [14] propose the Automated Water Extraction Index (AWEI), consisting of two forms: the AWEInsh and AWEIsh. The AWEIsh can effectively distinguish between water and shadow. Fisher et al. [11] construct the WI2015 by the linear discriminant analysis of surface reflectance data. Although this water index has a high extraction accuracy for Australia, its accuracy for other regions is still unknown. Wang et al. [15] constructed the MBWI, which significantly improves the water extraction accuracy in mountainous regions by mitigating mountain shadows. Hu et al. [16] explore the spectral characteristics of water with different sediment contents, and construct the WI2021. This method extracts water by enhancing water signals and suppressing reflectance differences in other ground objects based on the low-reflectance characteristics of water in the blue, green, red, near-infrared, and shortwave infrared bands. Wu et al. [17] construct the ratio water index (RWI), which can eliminate the influence of mixed pixels to a certain extent and make the water–land boundary more obvious.

Although a large number of water indexes have been proposed, each water body index has its own advantages and disadvantages, and no one water index can be applied to all scenarios with perfect performance. Many studies have integrated multiple water indexes to construct water extraction schemes, giving full play to the advantages of multiple water indexes and suppressing the disadvantages of each water index [18,19]. The most commonly used water extraction scheme in mid-latitude regions is the multi-index water extraction rule (MIWER) from Zou et al. [20]. This scheme combines a vegetation index

and water index according to a logical relationship. It limits the impact of vegetation on water through rules, greatly improves the accuracy of water, and has a better extraction effect on areas dominated by vegetation.

Machine learning classification methods, including supervised classification (such as K-Nearest Neighbors [21], Support Vector Machines [22–24], and Decision Trees/Random Forests [7,24–26]), and unsupervised classification (such as K-Means [27], Iterative Self-Organizing Data Analysis Technique [28], Density-Based Clustering [29], and Hierarchical Dynamic Clustering [30,31]), are another widely used approach for surface water extraction. Compared to unsupervised classification methods, supervised classification methods achieve higher water extraction accuracy. However, they rely on training samples, and their accuracy is highly dependent on the quality of these samples [32]. Therefore, how to quickly obtain high-quality training samples has become an important research direction for supervised classification-based surface water extraction. Recent studies frequently incorporate auxiliary data sources, such as OpenStreetMap (OSM) and surface water data products, to expedite the acquisition of training samples. For example, Zhang et al. [33] established an automatic water sample collection model based on OSM, which can automatically obtain high-precision water samples. With the rapid development of image recognition and classification methods, deep learning methods (such as convolutional neural networks [34,35], fully convolutional networks [36–38], U-Net [35,39], DeepLab [40,41], generative adversarial networks [24,42], and self-organizing maps [43]) are increasingly used in surface water extraction. These methods demonstrate strong recognition capabilities and high accuracy in water extraction. However, they require massive training samples and are complex and difficult to understand [44,45].

Overall, both water index methods and machine learning classification techniques have their respective advantages and limitations in water extraction. The water index can effectively extract water bodies through simple and easy band calculations. Therefore, its universality is deeply restricted by the mechanism. Additionally, determining the global optimal threshold is often challenging for large-scale surface water extraction due to the complexity of water spectral characteristics [46]. Machine learning classification methods have high water extraction accuracy, but these methods require researchers to have prior knowledge and collect training samples in advance. Therefore, for simpler scenes, it is advisable to use the water index method. However, the most appropriate water index should be carefully selected beforehand. In complex scenarios with significant heterogeneity in water spectral features, it is advisable to employ machine learning classification methods. In addition, we can also first transform the complex scenario into multiple simple scenarios and then extract surface water with an appropriate water index for each scenario.

Suspended particulate matter (SPM) in water refers to substances that are insoluble in water such as sediments, organic matter, and microorganisms, which can directly affect the water environment and water ecology. Compared with clean surface water, the spectral reflectance of water with a high SPM concentration shows a parabolic shape, with a trend of first increasing and then decreasing. And with the increase in the suspended particulate matter concentration, the reflectance peak shifts towards longer wavelengths, and the reflectance peak increases. According to the water index construction mechanism, the sensitivities to the SPM concentrations of different water indexes are different. Therefore, for areas with large spatial heterogeneity and a high SPM concentration, the water should first be classified according to the SPM concentration, and then the appropriate water index should be selected for each water type. Many studies have constructed SPM inversion methods and verified them with measured data. At present, the optical image inversion method mainly uses the red band reflectance value and the green band reflectance ratio or the near-red band reflectance value and the green band reflectance ratio. For example, the method used by Liu et al. [47] to invert the Yellow River Estuary achieved high accuracy.

The Yellow River is the fifth-longest river in the world, flowing through the Qinghai–Tibet Plateau, the Loess Plateau, and the North China Plain. The Yellow River accounts for only 2% of China's river runoff, but it needs to supply 12% of China's population with

water for production and domestic use and 15% of agricultural water for arable land [48]. Therefore, there is a severe contradiction between water supply and demand in the Yellow River Basin (YRB). Scientifically understanding the dynamic variations in surface water can provide available information for water resource management, agricultural water planning, and water resource optimization, significantly alleviating the supply–demand contradiction [49]. The characteristics of a large sediment content and spectral heterogeneity of surface water in the YRB pose significant challenges to surface water extraction [50]. Previous studies have established multi-index water extraction rules to achieve long-term water dynamic monitoring in the YRB, providing available information to understand the dynamic variation in surface water [3,19,51,52]. However, these methods typically rely on global segmentation thresholds and water extraction rules and have not considered the unique turbid surface water conditions of the YRB, resulting in numerous errors in surface water extraction. Additionally, the existing surface water dynamic monitoring research in the YRB lacks multi-scale comparative analysis.

Given this, this study fully considers the unique surface water characteristics of the YRB and establishes a surface water extraction method considering the suspended particulate matter concentration (SWE-CSPM) based on the concept of classification and grading. In addition, this study clarifies the surface water dynamic variation (1991–2023) in the YRB from four scales: the global scale, the secondary water resource zoning scale, the provincial scale, and the typical water bodies scale. The primary goals of this study are as follows: (1) verify the applicability of nine water indexes in the YRB. (2) Reveal the relationship between the SPM concentration and the water extraction accuracy of each water index and establish a surface water extraction method that accounts for the SPM concentration. (3) Describe the multi-scale surface water area changes in the YRB. This study provides an effective method for surface water extraction from multi-sediment rivers, and an important decision support for water resources management in the YRB.

2. Materials and Methods

2.1. Study Area

The Yellow River originates in the Bayan Har Mountains on the Qinghai–Tibet Plateau and flows eastward through Qinghai, Sichuan, Gansu, Ningxia Hui Autonomous Region, Inner Mongolia Autonomous Region, Shaanxi, Shanxi, Henan, and Shandong provinces, ultimately emptying into the Bohai Sea. The YRB spans approximately 5464 km and provides sufficient irrigation, revered as the cradle of Chinese civilization. It has 220 tributaries covering an area of 795,000 km^2. The mainstream is divided into upper, middle, and lower reaches according to the locations of Hekou Town and Taohuayu. The western source region is on the Qinghai–Tibet Plateau, with relatively high terrain covered with mountainous ice and snow landscapes. The central region lies on the Loess Plateau, with elevations between 1000 and 2000 m. It is prone to severe soil erosion, contributing to the main source of sediment in the Yellow River. The eastern region is part of the North China Plain, with an average elevation below 100 m. The YRB is divided into eight secondary water resource zonings based on topography and climate: Above Longyangxia, Longyangxia to Lanzhou City, Lanzhou City to Hekou Town, Hekou Town to Longmen County, Longmen County to Sanmenxia, Sanmenxia to Huayuankou, Below Huayuankou, and Interior Drainage Area (Figure 1). The YRB is one of the most severely eroded areas globally, with soil erosion affecting approximately 454,000 km^2, of which wind erosion affects about 117,000 km^2 and water erosion about 337,000 km^2. According to hydrological statistics from the Tongguan hydrological station, the annual average sediment transport from 1987 to 2020 was 466 million tons, with a sediment concentration of 18.1 kg/m^3. Serious soil erosion has transformed the Yellow River into a world-famous river with heavy sediment [53].

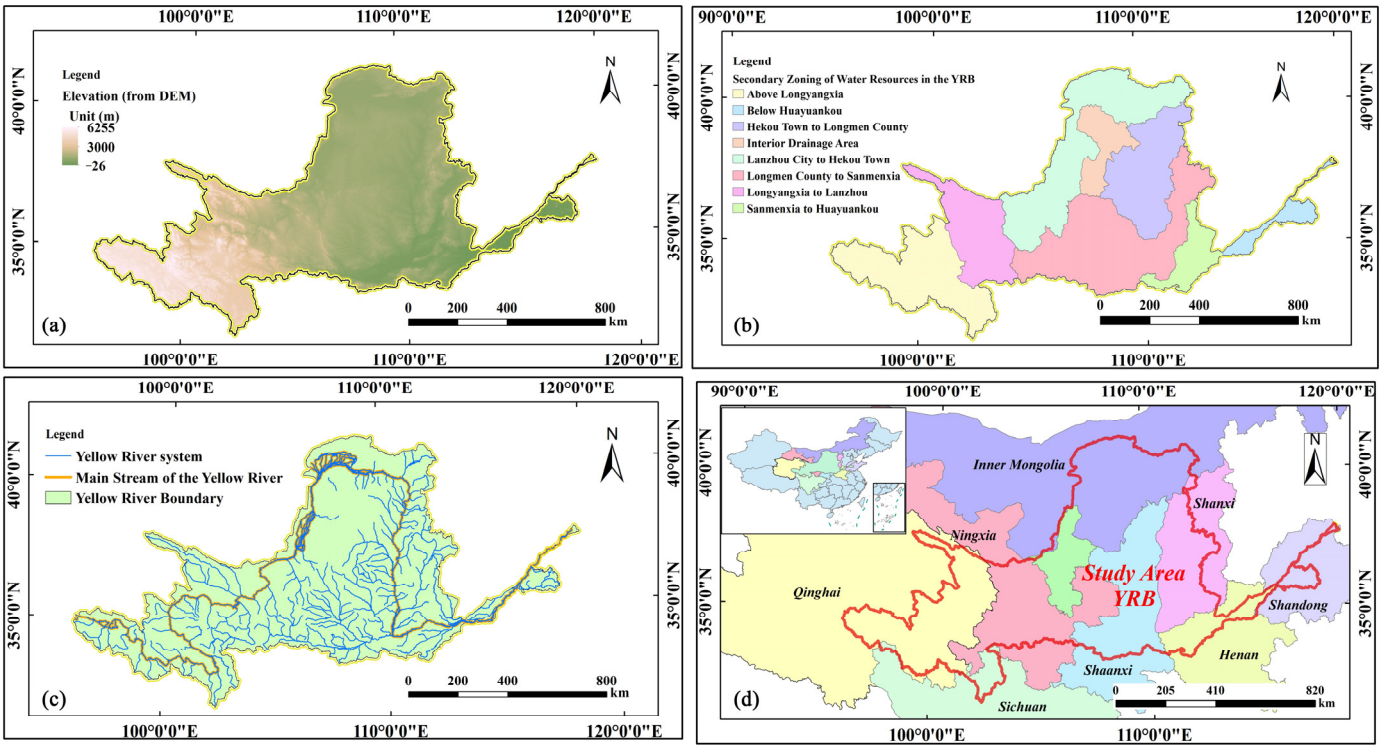

Figure 1. Study area in the YRB. (**a**) is the DEM of the Yellow River Basin, (**b**) is the secondary zoning map of the Yellow River Basin water resources, (**c**) is a schematic diagram of the Yellow River mainstream of the Yellow River Basin, and (**d**) is a provincial map of the Yellow River Basin.

2.2. Data

2.2.1. Remote Sensing Imagery

The Google Earth Engine (GEE) platform is used for data analysis and algorithm implementation. The Landsat series Tier 1 image collections are selected covering the YRB from 1991 to 2023 (a total of 70,642 scenes from Landsat 5, Landsat 7, and Landsat 8). In these images, the F-mask algorithm is used to eliminate invalid observation pixels, while the LEDAPS algorithm and LaSRC algorithm are used for atmospheric correction and geometric correction. In this study, auxiliary data (the Digital Elevation Model, DEM, and Sentinel 2) are chosen for further identification. The spatial resolution of the DEM is 30 m to eliminate the impact on mountain shadows. The JRC Dataset and Sentinel 2 image assist in sample collection and the evaluation of water extraction accuracy.

Figure 2 shows the spatial distribution of valid observations at the pixel scale for the YRB from 1991 to 2023. The northern part of the YRB has significantly more valid observations than the southern part, especially in the overlapping satellite areas. This is primarily due to the high latitude and mountainous terrain of the source region, which is more susceptible to cloud cover. Figure 3 displays the area proportion of valid observation counts for each year. Before 2000, the number of valid observations in most areas of the YRB is between 5 and 20. After 2000, this number is between 11 and 40, except for 2012.

2.2.2. Sample Point Selection

Following a stratified random sampling principle, more than 2900 samples (Figure 4) are visually interpreted and supplemented with Sentinel-2 MSI imagery and JRC data. These samples combine with 12 land cover types, including high-reflectance buildings, low-reflectance buildings, lakes/reservoirs, water in the upper reaches of the YRB, water in the middle reaches of the YRB, water in the lower reaches of the YRB, clouds, snow, building shadows, bare land, other shadows, and vegetation. For buildings, when selecting sample points, white, red, and bright blue buildings in the image are regarded as high-

reflective building elements. Dark gray and gray buildings in the image are regarded as low-reflective building elements.

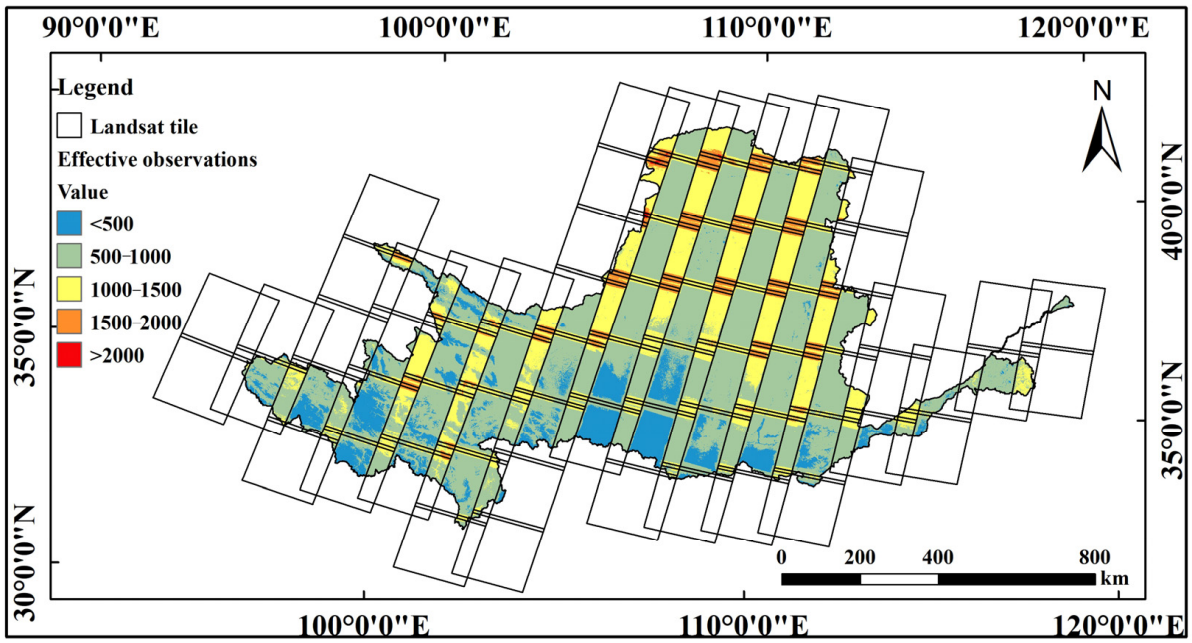

Figure 2. Spatial distribution of valid observations at the pixel scale in the YRB from 1991 to 2023.

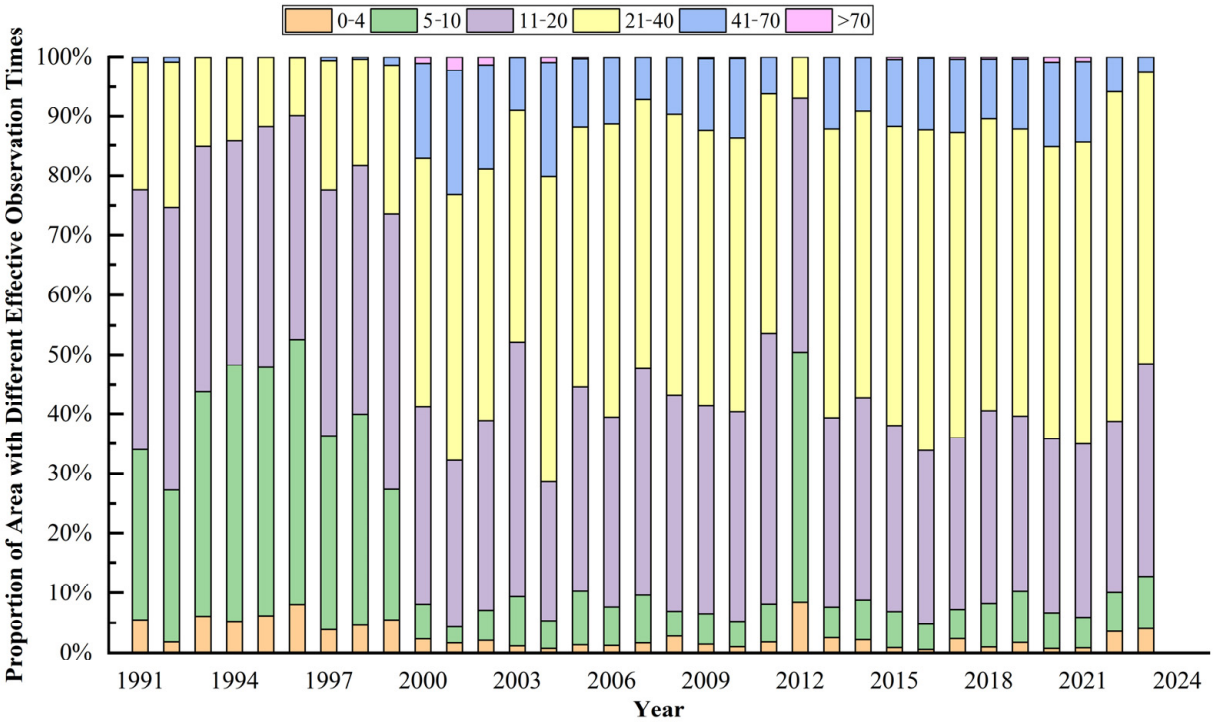

Figure 3. The percentage of pixels with effective observation in each segment. "0–4", "5–10", "11–20", "21–40", "41–70", and ">70" mean that the number of valid observations of a pixel in a year is between 0 and 4, 5 and 10, 11 and 20, 21 and 40, 41 and 70, and more than 70. This study further explores the proportion of the total number of pixels in each segment to the total number of pixels in the YRB.

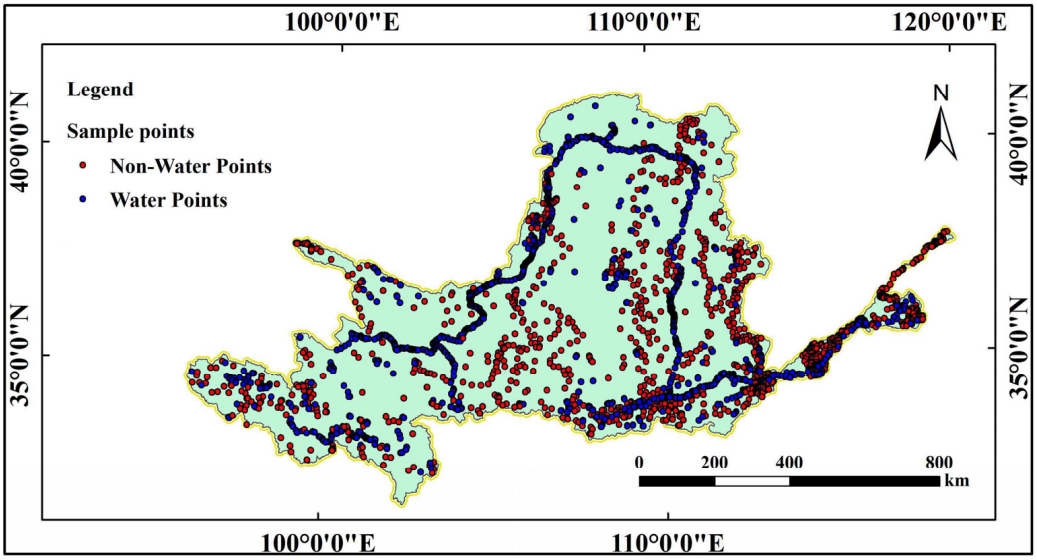

Figure 4. Spatial distribution of samples. For the subsequent accuracy evaluation, the study adopts a binary classification system (water and non-water).

Figure 5 shows the spectral characteristics of different land cover types. The water reflectance of the lower reaches is slightly higher than that of the upper reaches, middle reaches, and lake water. The reflectance peak of the lower reaches water is in the near-infrared band (Figure 5c), whereas the peaks for the upper reaches (Figure 5a) and middle reaches (Figure 5b) are in the red band, and for lakes and reservoirs (Figure 5d), in the green band. It can be inferred that the spectral reflectance of water increases with a higher sediment content, and the wavelength corresponding to the peak reflectance also increases. Shadows (Figure 5e,f) share similar spectral characteristics with water but exhibit a slightly lower reflectance. The spectral reflectance of vegetation (Figure 5g), bare land (Figure 5h), high-reflectance buildings (Figure 5l), low-reflectance buildings (Figure 5i), clouds (Figure 5j), and snow (Figure 5k) is significantly higher than that of water.

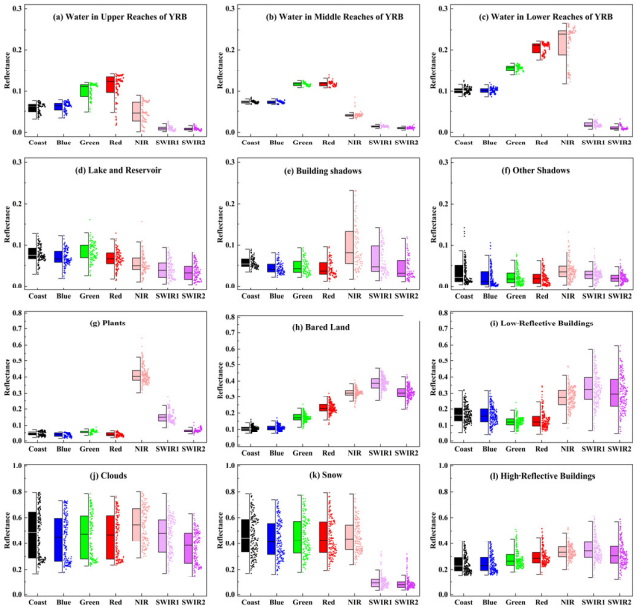

Figure 5. Spectral characteristics of different land cover types. Coast, Blue, Green, Red, NIR, SWIR1, and SWIR2 are the names of Band1-Coast aerosol, Band2-Blue, Band3-Green, Band4-Red, Band5-Near Infrared (NIR), Band6-Shortwave Infrared (SWIR)1, and Band7-Shortwave Infrared (SWIR)2 in Landsat 8 images, respectively.

3. Methods

Figure 6 presents the technical framework of this study, which consists of three parts: (1) analyze the relationship between the water index extraction accuracy and SPM concentration. Nine typical water indexes are selected for comparative analysis of their applicability in the YRB, and the correlation between the extraction accuracy of these indexes and SPM concentration is examined. (2) Establish a water extraction method considering the SPM concentration (SWE-CSPM). The SWE-CSPM is constructed according to the principle of classification and grading. Spectral characteristics and terrain slope are used for post-processing. (3) Multi-scale dynamic monitoring of surface water in the YRB. The surface water dataset of the YRB from 1991 to 2023 is made using the SWE-CSPM, and the water inundation frequency (WIF) model serves as an indicator to divide permanent, seasonal, and maximum water year by year. The dynamic changing characteristics of the surface water are analyzed from the global scale, the secondary water resource zoning scale, the provincial scale, and the typical water scale.

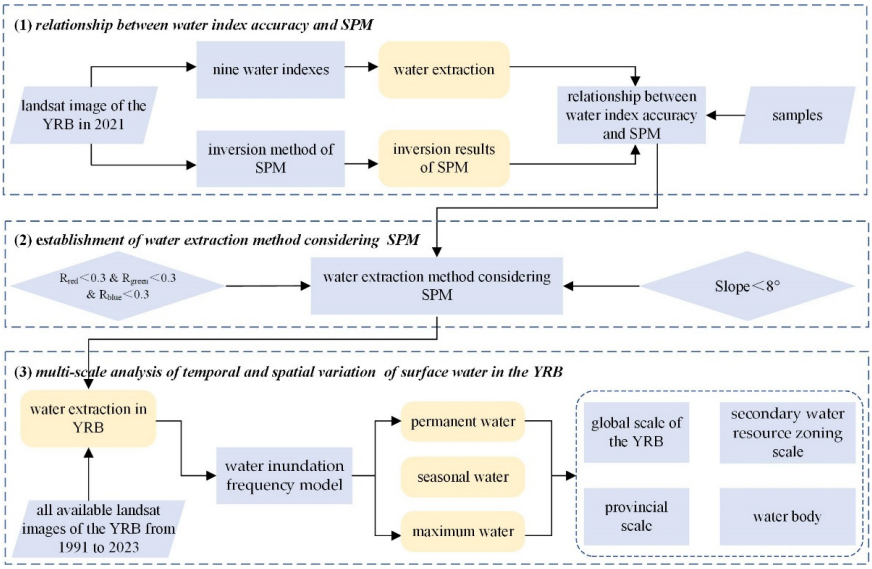

Figure 6. A flowchart of this study.

3.1. Water Indexes

Nine water indexes (NDWI, MNDWI, AWEInsh, AWEIsh, MBWI, WI2015, WI2021, RWI, and EWI) are selected to explore their applicability in the YRB. The details of the calculation for each water index are presented in Table 1.

Table 1. The nine water indexes selected in this study and their originations.

Water Index	Eq Id	Reference
$NDWI = \frac{\rho_{Green}-\rho_{NIR}}{\rho_{Green}+\rho_{NIR}}$	(1)	McFeeters et al. (1996) [10]
$MNDWI = \frac{\rho_{Green}-\rho_{MIR}}{\rho_{Green}+\rho_{MIR}}$	(2)	Xu (2005) [12]
$AWEI_{sh} = 4 \times (\rho_{Green} - \rho_{SWIR1}) - 0.25 \times \rho_{NIR} - 2.75 \times \rho_{SWIR2}$	(3)	Feyisa et al. (2014) [14]
$AWEI_{nsh} = \rho_{Blue} + 2.5 \times \rho_{Green} - 1.5 \times (\rho_{NIR} + \rho_{SWIR1}) - 0.25 \times \rho_{SWIR2}$	(4)	
$MBWI = 2 \times \rho_{Green} - \rho_{Red} - \rho_{NIR} - \rho_{SWIR1} - \rho_{SWIR2}$	(5)	Wang et al. (2018) [15]
$WI_{2021} = \frac{\rho_{Blue}+\rho_{Green}+\rho_{Red}-\rho_{NIR}-\rho_{SWIR1}-\rho_{SWIR2}}{\rho_{Blue}+\rho_{Green}+\rho_{Red}+\rho_{NIR}+\rho_{SWIR1}+\rho_{SWIR2}}$	(6)	Hu et al. (2022) [16]
$WI_{2015} = 1.7204 + 171 \times \rho_{Green} + 3 \times \rho_{Red} - 70 \times \rho_{NIR} - 45 \times \rho_{SWIR1} - 71 \times \rho_{SWIR2}$	(7)	Fisher et al. (2016) [11]
$RWI = \frac{\rho_{Green}+\rho_{Red}-2\times\rho_{NIR}-\rho_{SWIR2}}{\rho_{Green}+\rho_{Red}+2\times\rho_{NIR}+\rho_{SWIR2}}$	(8)	Wu et al. (2022) [17]
$EWI = \frac{\rho_{Green}-\rho_{SWIR1}+0.1}{\rho_{Green}+\rho_{SWIR1}} \times \left(\frac{\rho_{NIR}-\rho_{Red}}{\rho_{NIR}+\rho_{Red}} + 0.5\right)$	(9)	Wang et al. (2007) [13]

Notes: The labels of "ρ_{Blue}", "ρ_{Green} ", "ρ_{Red}", "ρ_{NIR}", "ρ_{MIR}", and "ρ_{SWIR}" represent the reflectance of blue, green, red, near-infrared, middle infrared, and short-wavelength infrared bands in Landsat series images.

3.2. SPM Concentration Retrieval

The SPM concentration is a crucial water quality parameter that is closely related to the spectral characteristics of water bodies. The SPM in the YRB is mainly suspended sediment. The SPM concentration inversion algorithm proposed by Liu et al. [47] is adopted in this study. The algorithm has been successfully applied to the inversion of SPM in the Yellow River Estuary [54]. The calculation model is as follows:

$$SPM = 10^{0.5897 \times \frac{\rho_{Red}}{\rho_{Green}} + 0.9864 \times \frac{\rho_{NIR}}{\rho_{Green}} + 1.3166} \quad (10)$$

where SPM represents the suspended particulate matter concentration, while ρ_{Green}, ρ_{Red}, ρ_{NIR} represent the surface reflectance of Band3-Green, Band4-Red, Band5-Near Infrared (NIR) in the Landsat 8 images, respectively.

Figure 7 shows the spatial distribution of the SPM concentration in the surface water of the YRB in 2021. Statistical analysis indicates that the water in the lower reaches has the highest SPM concentration (average 970 mg/L), followed by that in the middle reaches (average 700 mg/L), and the water in the upper reaches has the lowest concentration (average 630 mg/L).

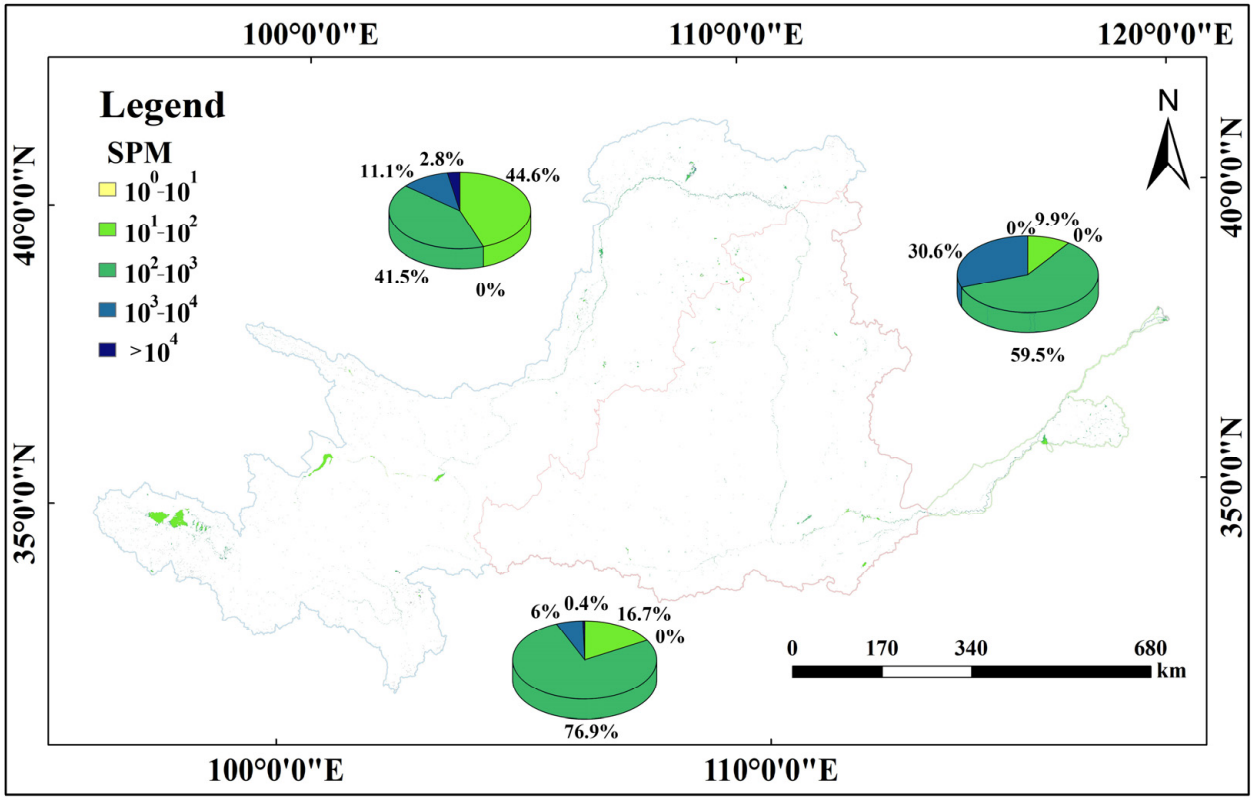

Figure 7. The spatial distribution of SPM concentration in surface water in 2021. The SPM concentration ranges from 0 to 10,000 mg/L in the YRB. However, that in lakes, reservoirs, and other water is lower than that in rivers.

3.3. Surface Water Extraction Method Considering SPM

The variation curves of different water indexes and SPM concentrations are illustrated in Figure 8. It is evident that the extraction accuracy of all water indexes decreases significantly with the increasing SPM. When the SPM is in the range of $[0, 10^{2.8}]$, all nine indexes achieve high extraction accuracy. Among them, the MBWI has the highest accuracy. When the SPM is in the range of $(10^{2.8}, 10^{3.1}]$, the extraction accuracy of the NDWI and MBWI decreases significantly. Among them, the WI2021 has the highest accuracy. When the SPM is in the range of $(10^{3.1}, 10^{4}]$, the AWEInsh significantly outperforms the other water indexes.

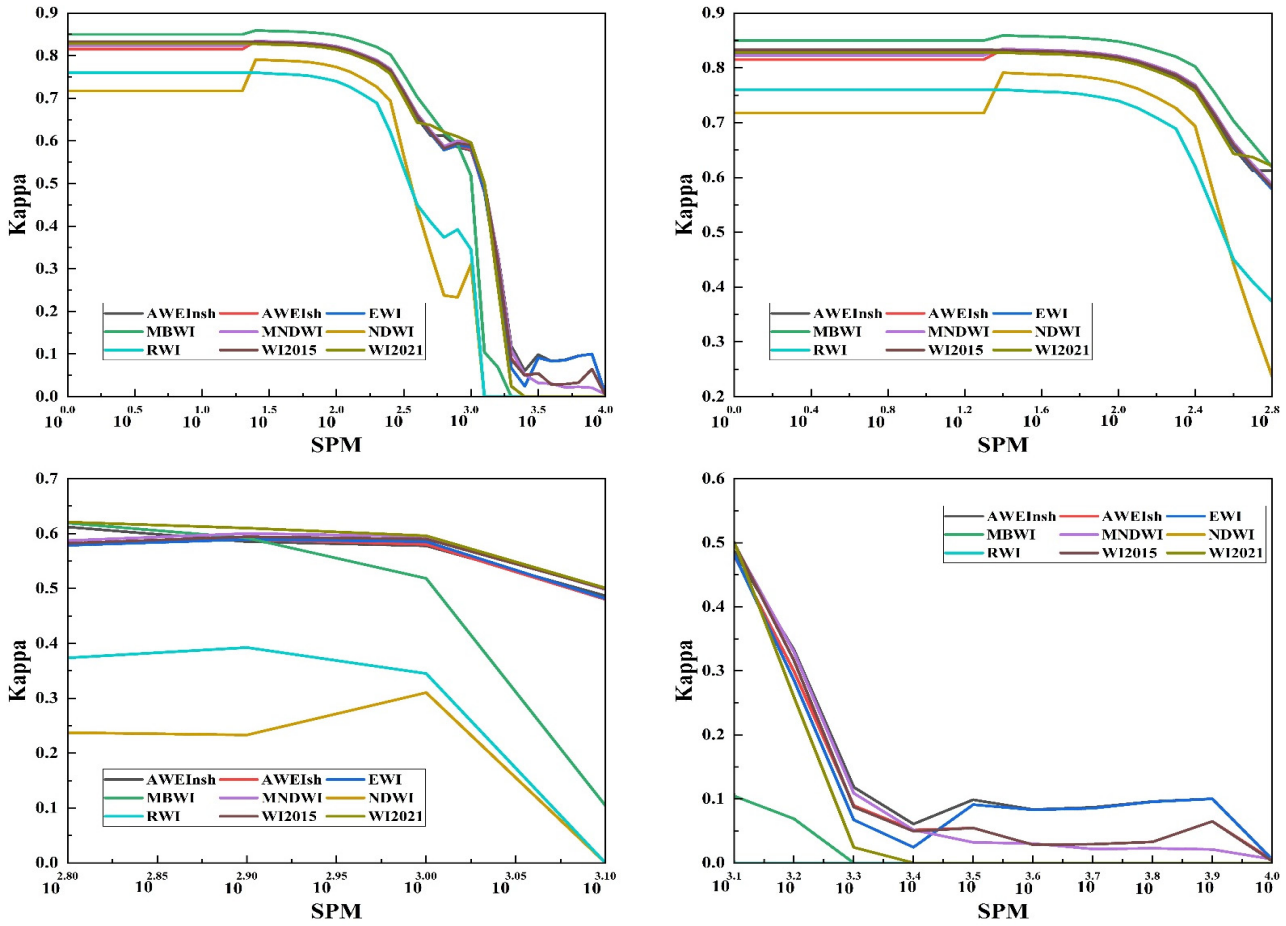

Figure 8. Change curve of water extraction accuracy (kappa coefficient) of each water index with the increase in SPM.

Based on the relationship between the extraction accuracy of each water index and SPM concentration, the SWE-CSPM is proposed. The model is as follows:

$$SWE_{SPM} = \begin{cases} MBWI \geq -0.15 & \left(0 \leq SPM \leq 10^{2.8}\right) \\ WI_{2021} \geq 0.04 & \left(10^{2.8} \leq SPM \leq 10^{3.1}\right) \\ AWEI_{nsh} \geq 0.05 & \left(10^{3.1} \leq SPM \leq 10^{4}\right) \end{cases} \quad (11)$$

When the SPM concentration of surface water is in the range of $[0, 10^{2.8}]$, surface water is identified based on the index model $MBWI \geq -0.15$. When the SPM concentration is in the range of $(10^{2.8}, 10^{3.1}]$, the index model $WI_{2021} \geq 0.04$ is used. When the SPM concentration is in the range of $(10^{3.1}, 10^{4}]$, the index model $AWEI_{nsh} \geq 0.05$ is used. These threshold parameters are determined by repeated tests.

Although this scheme can largely eliminate the interference of buildings and vegetation on water extraction, snow and mountain shadows are still easily misidentified as water. To solve these interference factors, this study constructs post-processing rules based on the spectral characteristics of different land cover types in Section 2.2.2. High-reflective features are excluded using the rule that the spectral reflectance of the red, green, and blue bands is less than 0.3. Furthermore, we exclude mountain shadows by applying the slope rule of less than 8°, which is in line with existing research findings.

3.4. Accuracy Evaluation

In order to scientifically evaluate the extraction accuracy of the water index, this study adopts the traditional accuracy evaluation criteria based on a confusion matrix,

including the overall accuracy (OA), kappa coefficient (kappa), commission errors (CEs), and omission errors (OEs). These formulas are as follows:

$$OA = \frac{\sum O_{ii}}{N} \tag{12}$$

$$Kappa = \frac{\frac{\sum_{i=1}^{k} O_{ii}}{N} - \sum_{i=1}^{k}\left(\frac{\sum_{j=1}^{k} O_{ij}}{N} \cdot \frac{\sum_{j=1}^{k} O_{ji}}{N}\right)}{1 - \sum_{i=1}^{k}\left(\frac{\sum_{j=1}^{k} O_{ij}}{N} \cdot \frac{\sum_{j=1}^{k} O_{ji}}{N}\right)} \tag{13}$$

$$CE_i = \frac{\sum_{j=1 j \neq i}^{k} O_{ji}}{\sum_{j=1}^{k} O_{ji}} \tag{14}$$

$$OE_i = \frac{\sum_{j=1 j \neq i}^{k} O_{ij}}{\sum_{j=1}^{k} O_{ij}} \tag{15}$$

where O represents the confusion matrix, N represents the total number of samples, O_{ij} represents the element in the i-th row and j-th column of the confusion matrix, O_{ji} represents the element in the j-th row and i-th column of the confusion matrix, and k is the number of categories.

In addition, this study also combines the MIWER by Zou et al. [19] for verification. The formula of MIWER is as follows:

$$\begin{gathered} MIWER = ((MNDWI > EVI)\ or\ (MNDWI > NDVI))\ and\ (EVI < 0.1) \\ EVI = 2.5 \times \frac{\rho_{NIR} - \rho_{Red}}{\rho_{NIR} + 6 \times \rho_{Red} - 7.5 \times \rho_{Blue} + 1} \\ NDVI = \frac{\rho_{NIR} - \rho_{Red}}{\rho_{NIR} + \rho_{Red}} \end{gathered} \tag{16}$$

among those, MNDWI is the water index, EVI and NDVI are the vegetation indexes. ρ_{Blue}, ρ_{Red}, ρ_{NIR} represent the reflectance of the blue, red, and near-infrared bands in the Landsat series images, respectively.

3.5. Water Inundation Frequency (WIF)

The WIF is a universal indicator that can monitor long-term changes in water. The WIF refers to the proportion of the number of times a pixel is judged to be water in a year to the total number of valid observations in that year. This study uses the WIF to classify surface water bodies into the largest, permanent, and seasonal water. The WIF is usually expressed as a percentage, and the calculation formula is shown below:

$$WIF = \frac{W}{N} \times 100\% \tag{17}$$

where W represents the count of a pixel identified as water. N represents the count of valid observations for a pixel in a year. Based on the existing research [52,55,56], the $WIF > 25\%$, $25\% < WIF \leq 75\%$, $WIF \geq 75\%$ and are defined as the maximum, seasonal, and permanent water, respectively.

4. Results

4.1. Water Extraction Accuracy

Based on the synthetic images in 2021, Appendix A Figure A1 illustrates the surface water extraction of various methods. Table 2 presents the water extraction accuracy. Among the nine water indexes, the MBWI demonstrates the highest accuracy, followed by the AWEInsh and WI2021, while the NDWI shows the lowest accuracy. Compared with the nine water indexes and the MIWER [19,55], the SWE-CSPM achieves the highest accuracy. The detailed information on the SWE-CSPM extraction accuracy is that the overall accuracy (OA) is 95.44% and the kappa coefficient is 90.65%. The overall accuracy of the SWE-CSPM increases by 2.84% and 1.44% compared to the MBWI and MIWER, respectively, while

the kappa coefficient increases by 5.64% and 2.88%. Notably, both the SWE-CSPM and the MIWER significantly reduce the commission error (CE), albeit with a slight increase in the omission error (OE). The reason for this improvement may be that the utilization of slope data and spectral characteristics of ground features in the post-processing stage effectively decreases the interference of high-reflective features and mountain shadows. To further validate the effectiveness of our approach, we also evaluate the accuracy before post-processing. The overall accuracy, kappa coefficient, commission error (CE), and omission error (OE) are 94.00%, 87.74%, 6.59%, and 7.45%, respectively. Both the overall accuracy and kappa coefficient exceed those of the individual water indexes, indicating that the proposed SWE-CSPM can effectively improve the extraction accuracy of surface water in the YRB.

Table 2. Extraction accuracy of surface water based on 2021 synthetic images using various methods.

Water Extraction Method	Overall Accuracy	Kappa	Commission Error	Omission Error
AWEInsh	91.71%	83.18%	11.76%	6.95%
AWEIsh	90.92%	81.52%	11.72%	9.13%
EWI	91.31%	82.33%	11.43%	8.46%
MBWI	92.60%	84.98%	10.35%	6.45%
MNDWI	91.49%	82.79%	12.70%	6.20%
NDWI	85.85%	71.75%	21.59%	7.54%
RWI	86.82%	73.61%	20.01%	7.62%
WI2015	91.45%	82.65%	11.70%	7.71%
WI2021	91.53%	82.81%	11.80%	7.37%
SWE-CSPM	95.44%	90.62%	2.58%	8.21%
MIWER	94.00%	87.74%	6.59%	7.45%

Figure 9 illustrates the water extraction of various methods in high mountainous regions (Scenario 1). This region is located at the source of the Yellow River, and the ice–snow and mountain shadows are the main interference factors for surface water extraction. It is obvious that the SWE-CSPM outperforms the nine water indexes and the MIWER, effectively decreasing the misclassification of shadow and ice–snow features as water. Figure 10 shows the water extraction of various methods in urban regions (Scenario 2). This region exhibits complex surface features with significant interferences, such as high-reflective buildings, low-reflective buildings, and building shadows. The SWE-CSPM demonstrates the most effective water extraction method, whereas the NDWI and AWEIsh performed poorly, with numerous ground objects misclassified as water. The water areas of the full image, Scenario 1, and Scenario 2 are shown in Figure 11.

4.2. Surface Water Area Changes in the YRB

4.2.1. Surface Water Area Changes at the Global Scale in the YRB

Figure 12 illustrates the area changes in the maximum, permanent, and seasonal water at the global scale of the YRB from 1991 to 2023. It is evident that the maximum water has exhibited a fluctuating downward trend during the study period, but the decreasing range is small. The area of permanent water initially decreases (1991–2001) and then increases (2001–2023), showing an overall uptrend. The seasonal surface water area exhibits a downtrend, with a reduction of 624 km^2 by 2023 compared to 1991. The average annual maximum water area is 8414 km^2, accounting for only 1.05% of the total area of the YRB, which is significantly lower than that in the Yangtze River Basin (approximately 2%) [56] and Hai River Basin (approximately 1.3%) [57]. This indicates that the visible surface water in the YRB is relatively small, closely due to the region's climatic characteristics of low precipitation and high evaporation. The average annual areas of permanent and seasonal water are 4662 km^2 and 3751 km^2, respectively, comprising 55% and 45% of the maximum surface water area, indicating that permanent water dominates in the YRB.

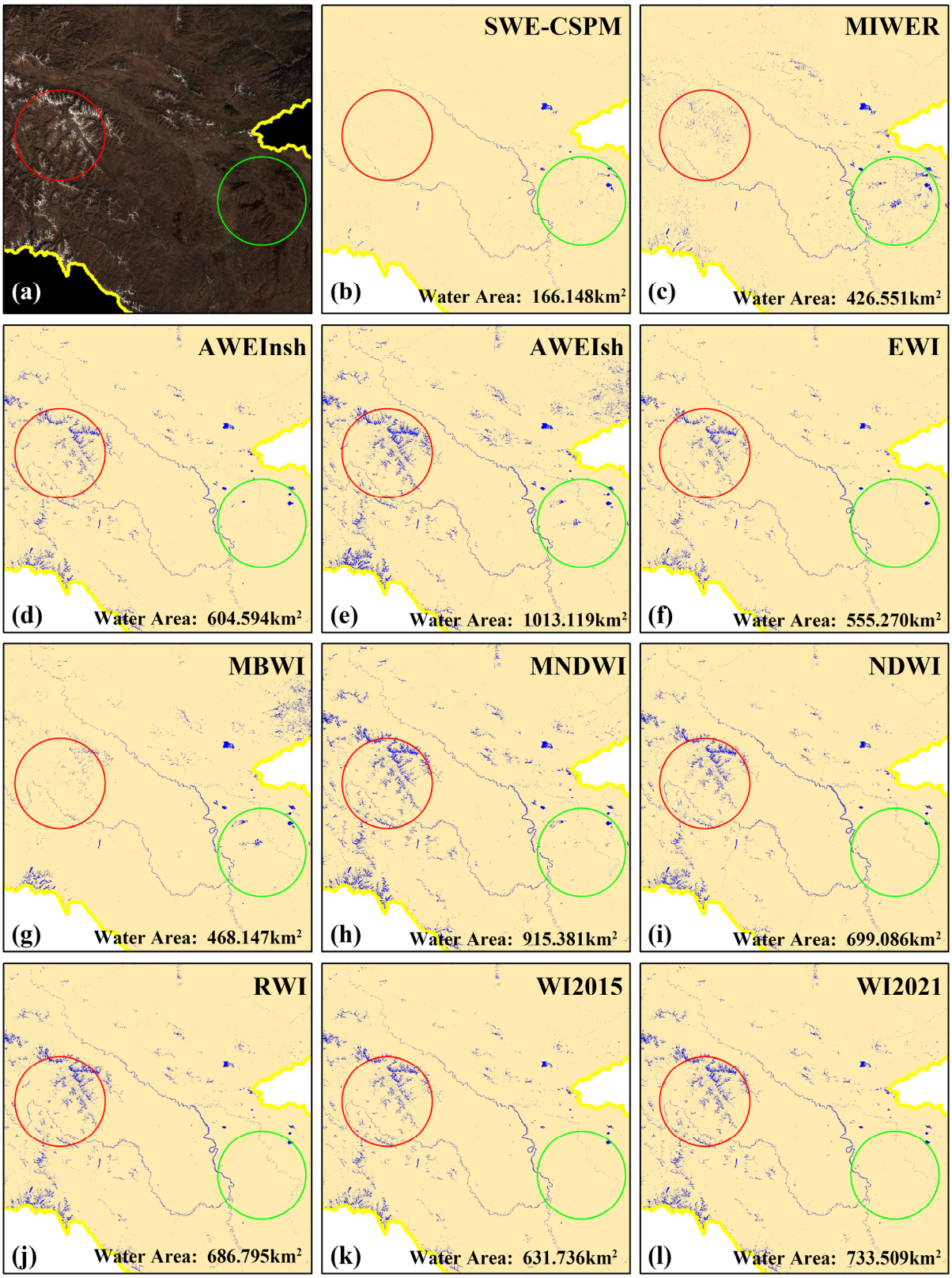

Figure 9. Surface water extraction of various methods in high mountain regions. The red circle is the area of ice–snow and the green circle is the area of shadow. (**a**) Landsat 8 true colour images of the area. (**b**–**l**), respectively the extraction effect of SWE-CSPM MIWER, AWEInsh, AWEIsh, EWI, MBWI, MNDWI, NDWI, RWI, WI2015 and WI2021.

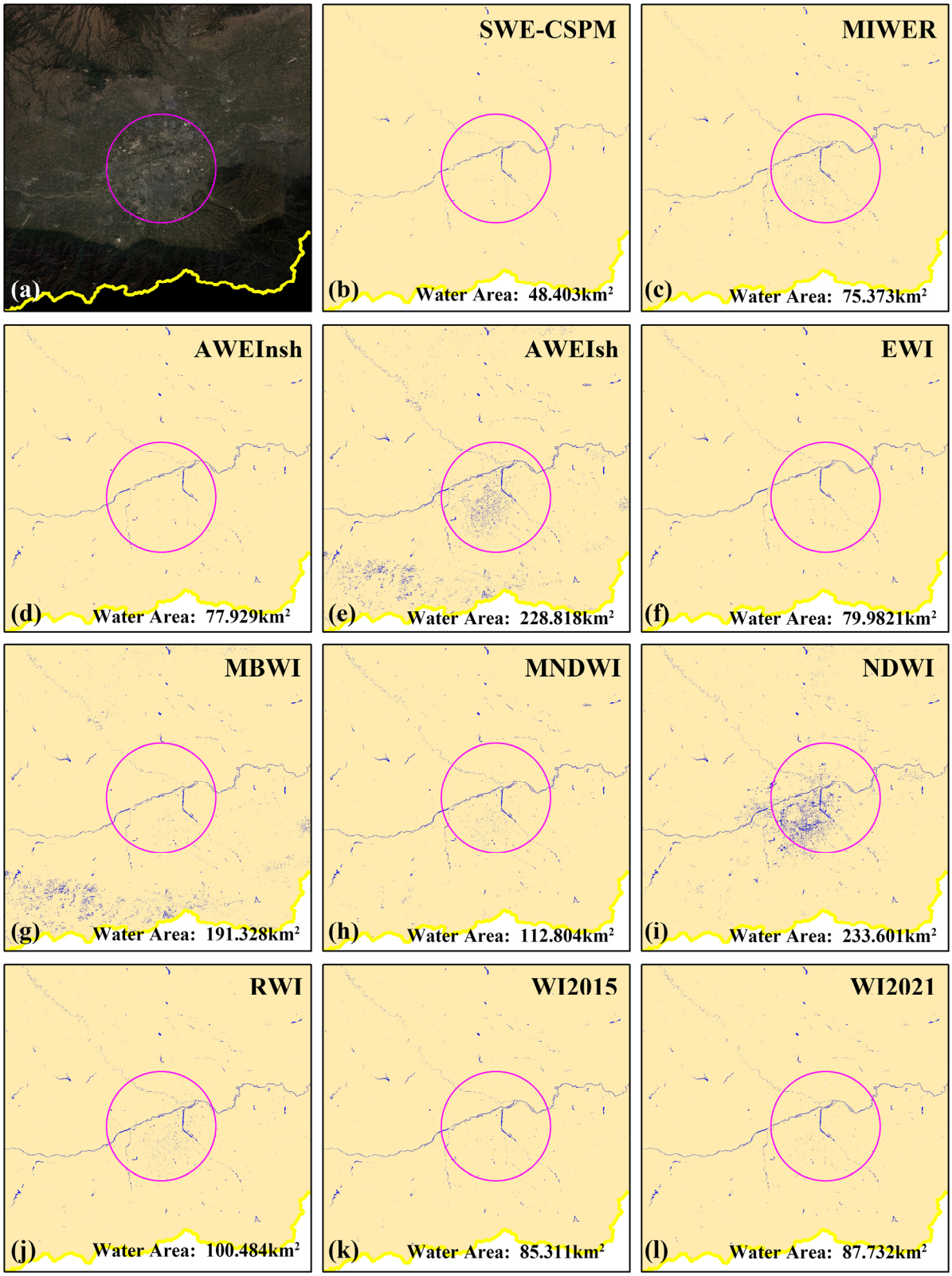

Figure 10. Surface water extraction of various methods in urban areas. The purple circle is the area of buildings. (**a**) Landsat 8 true colour images of the area. (**b**–**l**), respectively the extraction effect of SWE-CSPM MIWER, AWEInsh, AWEIsh, EWI, MBWI, MNDWI, NDWI, RWI, WI2015 and WI2021.

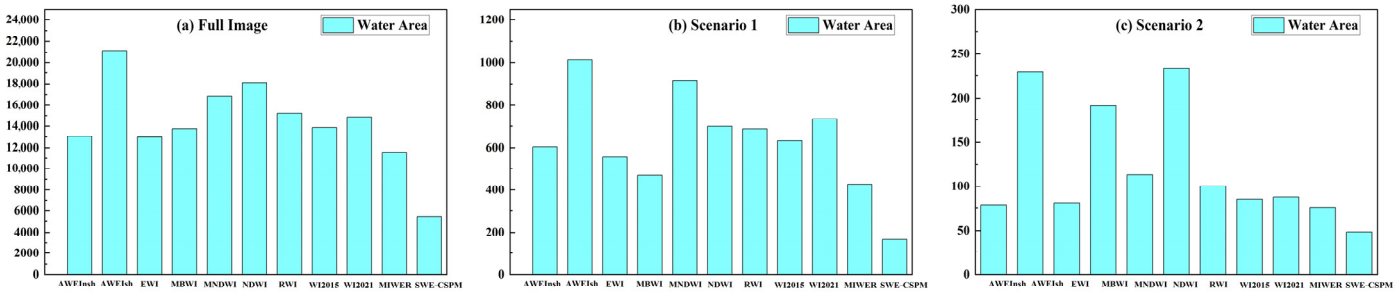

Figure 11. The water area of full image, Scenario 1, and Scenario 2.

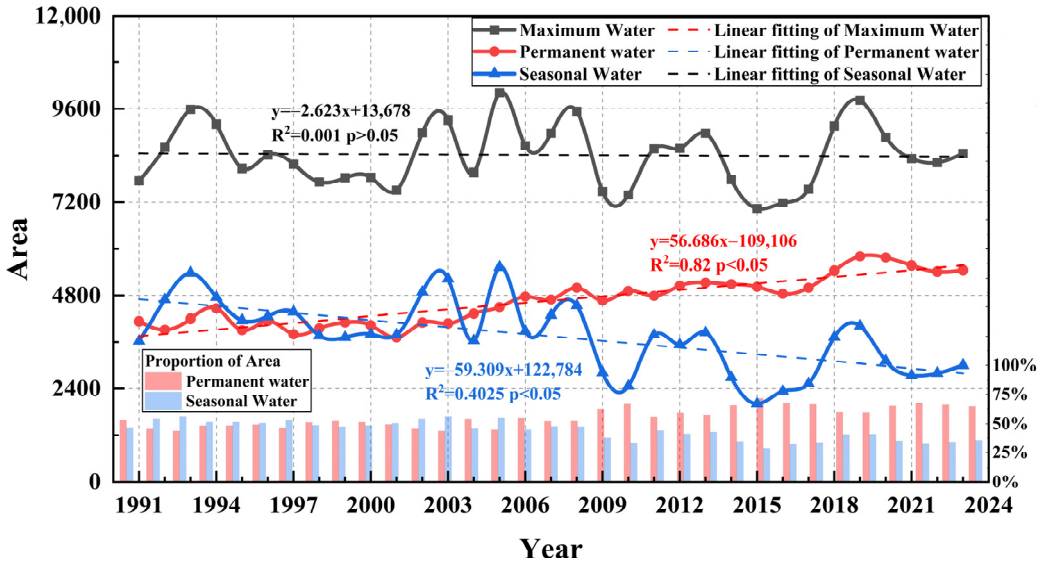

Figure 12. Surface water area changes in maximum, permanent, and seasonal water at the global scale in the YRB (1991–2023). The black curve and dashed line represent the area change trend and linear fitting relationship of the maximum water; the red curve and dashed line represent the area change trend and linear fitting relationship of the permanent water; the blue curve and dashed line represent the area change trend and linear fitting relationship of the seasonal water.

4.2.2. Surface Water Area Changes at the Secondary Water Resource Zoning Scale

Water resource zoning refers to the scientific division of water resources in a certain area based on the natural distribution characteristics of water resources, social and economic conditions, and ecological and environmental needs. Figure 13 shows the maximum, permanent, and seasonal water area changes for each secondary water resource zoning. The maximum surface water area at the secondary water resource zoning scale of the YRB is as follows: Above Longyangxia > Lanzhou City to Hekou Town > Below Huayuankou > Longmen County to Sanmenxia > Longyangxia to Lanzhou City > Sanmenxia to Huayuankou > Hekou Town to Longmen County > Interior Drainage Area. Above Longyangxia has the largest maximum surface water area, due to it being a major water-producing area with abundant water resources and widespread rivers and lakes. The Interior Drainage Area has the smallest water area, primarily due to it being part of the Mu Us Desert, characterized by an arid climate with low precipitation and high evaporation.

Except for the Interior Drainage Area, the permanent surface water area in other secondary water resource zonings increases slowly to varying degrees, with the growth rate from large to small as follows: Above Longyangxia > Lanzhou City to Hekou Town > Be-low Huayuankou > Longmen County to Sanmenxia > Sanmenxia to Huayuankou > Hekou Town to Longmen County > Longyangxia to Lanzhou City > Interior Drainage Area. The growth rate ranges from 0 to 12 km^2/a. Overall, the western and southern secondary water resource zonings exhibit higher growth rates of permanent surface water

area compared to the central and northern zonings. Seasonal surface water areas in all secondary water resource zonings show a fluctuating downward trend, and the downward rate of Longmen County to Sanmenxia is the highest. In 2022, the seasonal surface water areas in Lanzhou City to Hekou Town and the Interior Drainage Area exhibit sudden increases, which are likely due to significant precipitation increases in the northwest region of the YRB.

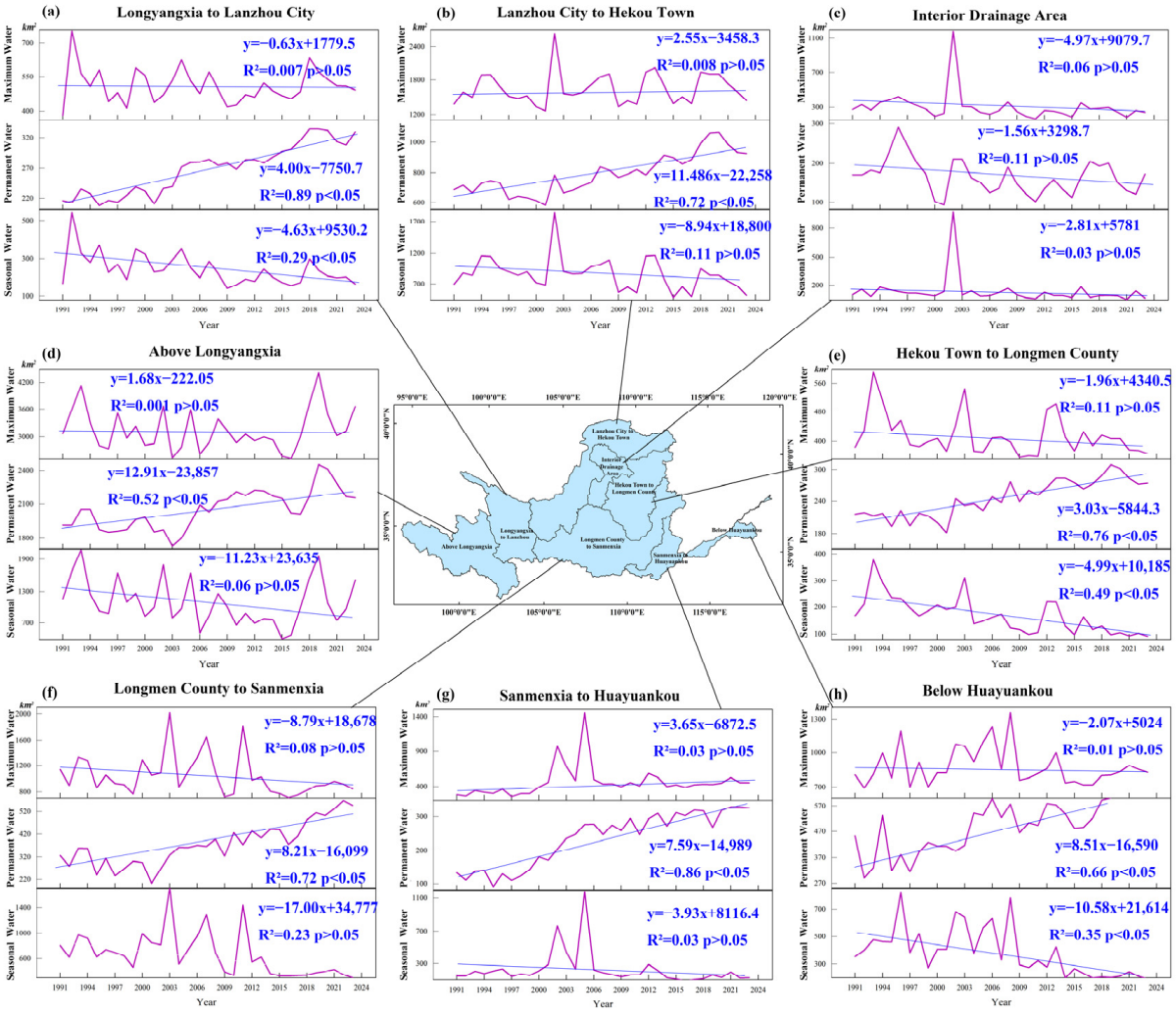

Figure 13. Surface water area changes in maximum, permanent, and seasonal surface water for each secondary water resource zoning (1991–2023). (**a**–**h**) respectively represent the three statistical water areas in Longyangxia to Lanzhou City, Lanzhou City to Hekou Town, Interior Drainage Area, Above Longyangxia, Hekou Town to Longmen County, Longmen County to Sanmenxia, Sanmenxia to Huayuankou and Be-low Huayuankou.

4.2.3. Surface Water Area Changes at the Provincial Scale

Figure 14 illustrates the changes in the maximum, permanent, and seasonal water areas for the nine provinces within the YRB. It is crucial to note that the provinces considered in this study only represent the areas within the YRB, not the entire provincial units. It is evident that, for the maximum surface water, only Shandong Province, Inner Mongolia Autonomous Region, and Qinghai Province exhibit a slow increase from 1991 to 2023. Other provinces show a downtrend, with Shaanxi Province having the highest rate of decrease. For permanent surface water, all provinces exhibit a trend of increasing in different degrees, with Qinghai Province having the highest growth rate at 15.16 km^2/a. Sichuan Province has the smallest water area and the smallest annual growth rate of only 0.096 km^2/a. For

seasonal surface water, all provinces exhibit varying degrees of fluctuating decreases, with Shaanxi Province showing the highest rate of decrease.

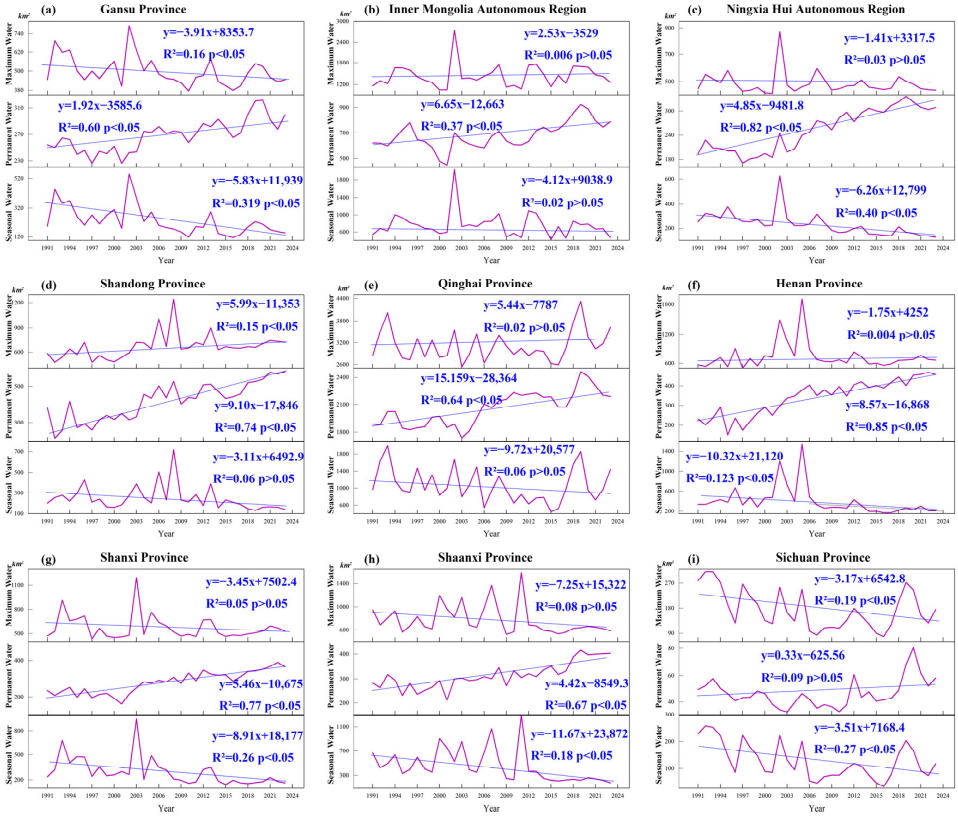

Figure 14. Surface water area changes in maximum, permanent, and seasonal surface water areas for the nine provinces within the YRB. (**a**–**i**) respectively represent the three statistical water areas in Gansu Province, Inner Mongolia Autonomous Region, Ningxia Hui Autonomous Region, Shandong Province, Qinghai Province, Henan Province, Shanxi Province, Shaanxi Province and Sichuan Province.

4.2.4. Surface Water Area Changes at the Typical Water Bodies

This study selects five typical lakes (Zhaling Lake, Eling Lake, Wuliangsuhai, Hongjiannao, and Dongping Lake) from the upper, middle, and lower reaches to analyze their surface water area changes. Zhaling Lake and Eling Lake are two typical natural lakes in the source region of the YRB. Wuliangsuhai and Hongjiannao are representative of natural lakes in the middle reaches of the Yellow River. Wuliangsuhai is located in Urad Front Banner, Bayannur City, Inner Mongolia Autonomous Region. It is a large multifunctional lake with high ecological value, rare in desert and semi-desert regions globally. To maintain the ecosystem health in the Wuliangsuhai, the Inner Mongolia Autonomous Region has provided 3.648 billion m^3 of ecological water replenishment since 2007 [58]. Hongjiannao is located between Shenmu City in Shaanxi Province and Ejin Horo Banner in the Inner Mongolia Autonomous Region. It is the largest desert lake in China. To improve the water environment of the Hongjiannao Nature Reserve, 1 million m^3 of ecological water replenishment has been provided since 2017 from the Erdos Zhasake Reservoir. Dongping Lake, located in Dongping County, Shandong Province, is the only significant flood storage area in the lower reaches of the Yellow River. It is a significant hub for the Eastern Route of the South-to-North Water Diversion Project and the Beijing–Hangzhou Grand Canal.

Figure 15 illustrates the surface water area changes in the five typical lakes. The processes of surface water area changes differ among lakes. For the maximum water, Zhaling Lake exhibits an initial decrease (1991–2001) followed by an increase (2001–2023). Eling Lake exhibits fluctuating changes initially (1991–2001), followed by an increase

(2001–2023). Wuliangsuhai exhibits overall fluctuating changes, with relatively small variations. Hongjiannao exhibits an initial decrease (1991–2015) followed by an increase (2015–2023). Dongping Lake exhibited fluctuating changes before 2012, with an initial decrease followed by an increase from 2012 to 2023.

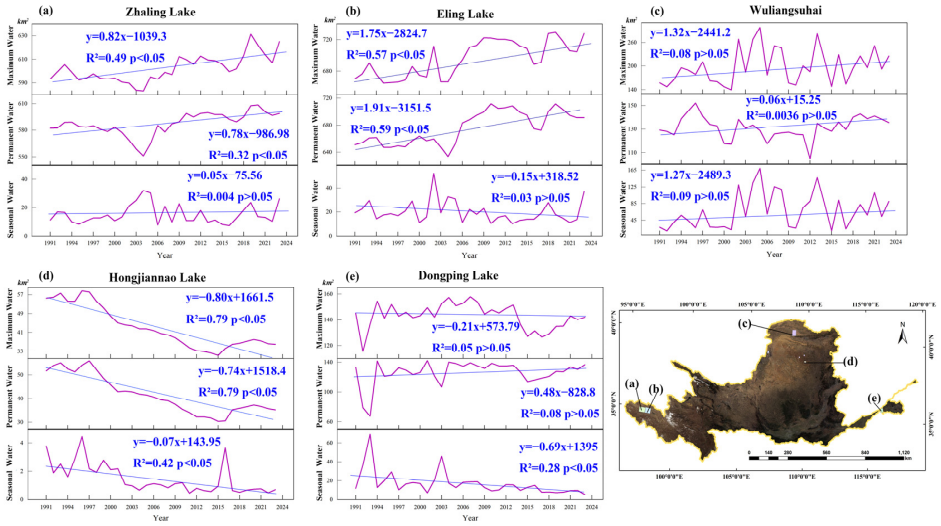

Figure 15. Surface water area changes in maximum, permanent, and seasonal water for typical five lakes in the YRB. (**a**–**e**) respectively represent the three statistical water areas of Zhaling Lake, Eling Lake, Wuliangsuhai, Hongjiannao Dongping Lake.

The changes in the permanent water areas of the five lakes generally mirror those of the maximum water areas, indicating that permanent water dominates the changes in the maximum surface water areas. For seasonal water, the changes are relatively small, but the variation trends among the lakes are slightly different. Zhaling Lake and Wuliangsuhai show a slow uptrend, while Eling Lake, Hongjiannao, and Dongping Lake exhibit a slow downtrend.

5. Discussion

5.1. The Applicability of Water Indexes in the YRB

The surface water of YRB has the characteristics of a large sediment content, and the sediment content has large spatial heterogeneity. They pose a great extraction challenge to surface water. The accuracy of the nine typical water indexes is in order from large to small (Table 2) as follows: MBWI > AWEInsh > WI2021 > MNDWI > WI2015 > EWI > AWEIsh > RWI > NDWI. Therefore, it is recommended to prioritize the MBWI, AWEInsh, and WI2021 when using a single water index to extract surface water in the entire YRB. All nine water indexes have good extraction results in the mainstream of the YRB, tributaries with large river widths, and large lakes and reservoirs. However, for narrow rivers and tiny streams, the identification effect of each water index is poor due to the limitations of Landsat images' spatial resolution (Appendix A Figure A1). Therefore, when extracting surface water in the northwest region of the YRB with narrow rivers and tiny streams, it is recommended to use images with higher spatial resolution such as Sentinel, GF, and Worldview images. As shown in Figure 9, compared with other water indexes, the MBWI can more effectively distinguish between water and ice–snow (Figure 9g). For the areas covered with ice–snow (such as the source region of the YRB), it is recommended to prioritize the MBWI for surface water extraction. In Figure 10, the MNDWI, AWEInsh, and WI2021 can effectively decrease the interference of built-up areas to water extraction (Figure 10d,h,l). Therefore, for areas containing built-up areas, it is recommended to prioritize the MNDWI, AWEInsh, and WI2021.

5.2. The Effectiveness of the SWE-CSPM

The spectral characteristics of water are usually related to their various components. As shown in Figure 5, the spectral characteristics of water in different sections of the YRB undergo significant changes with the sediment content. Figure 8 illustrates that the most applicable water index for surface water with different SPM concentrations is also different. Therefore, based on the concept of classification and grading, surface water is initially categorized into several types according to the SPM concentration. Subsequently, the optimal water index is chosen for each type of water to facilitate water extraction. The scheme is theoretically reasonable and feasible. This study introduces the SPM concentration inversion algorithm proposed by Liu et al. [47], which has been successfully applied to the inversion of the SPM concentration in the Yellow River estuary and extended to the whole YRB in this study. Appendix A Figure A1 and Table 2 demonstrate that in terms of water extraction accuracy, the SWE-CSPM significantly outperforms the nine water indexes and the MIWER. The above experimental results reveal that the SWE-CSPM is effective in improving the extraction accuracy of surface water throughout the YRB. The main reason is that this SWE-CSPM simplifies complex surface water into multiple single types, which improves the separation of water from other surface features and reduces the commission error.

5.3. Spatiotemporal Variation Characteristics of Water Area

This study analyzes the change characteristics of the water area in the YRB at the global scale, the secondary water resource zoning scale, the provincial scale, and the typical water scale. At the global scale, the maximum water area fluctuates slightly downward, the permanent water area shows an uptrend, and the seasonal water area shows a downtrend annually. These trends are generally consistent with the results of Zhang et al. [3] and Hu et al. [55], but the water area is slightly smaller than that of Hu et al. The main reason for the difference is that the SWE-CSPM improves the surface water extraction accuracy and reduces the commission error. According to the previous results [59,60], the permanent water area has increased annually, mainly due to the increase in precipitation and glacial meltwater caused by climate warming. The seasonal water area shows a downtrend annually, which may be due to the transformation of some seasonal water into permanent water. This shift may be attributed to the construction of reservoir projects and the replenishment of lake wetlands [52]. These changes greatly indicate the substantial spatial heterogeneity of surface water.

At the secondary water resource zoning scale, the permanent water area of the Interior Drainage Area remains stable, while other zones show an uptrend. Among them, the permanent water area of Above Longyangxia has the largest growth rate and the largest maximum water area. The reason is that the zoning is the main water source of the YRB, and the water resources are abundant. At the provincial scale, the permanent water area of each province shows an increasing trend to varying degrees. Among them, the water area of Qinghai Province has the largest growth rate, and the reason is similar to that of the secondary water resource zonings, both of which have large lakes in the upper reaches. The seasonal water area of each province shows a fluctuating downtrend. In terms of the maximum water area, only Shandong Province, Inner Mongolia Autonomous Region, and Qinghai Province have a slow increase; the rest of the provinces show a downtrend.

At the typical water scale, there are great differences in the process of water area change in five lakes. Over the past decade, Zhaling Lake, Eling Lake, Wuliangsuhai Lake, Hongjiannao, and Dongping Lake have all shown an uptrend in their permanent water area and maximum water area. On the one hand, climate change has led to an increase in the natural inflow runoff of lakes. On the other hand, water conservancy management departments actively promote river and lake protection policies. Through these policies, numerous ecological water replenishment projects have been implemented for rivers and lakes that are important for ecological functions and whose water areas have seriously shrunk.

5.4. Limitation and Future Work

This study analyzes the dynamic variations in surface water in the YRB at various scales but has not yet conducted an in-depth analysis of the driving mechanisms of climate change and human activities on the spatiotemporal variations at different scales. In addition, this study has not yet involved research on surface water area prediction, early warning, and dynamic changes in water storage. In subsequent studies, we will plan to use higher-resolution terrain data, radar imagery, and optical imagery to conduct a surface water classification, which includes the mainstream, first-level tributaries, second-level tributaries, reservoirs, natural lakes, ponds, wetlands, and more. After analyzing the spatiotemporal variation characteristics of each type of water, we will combine meteorological data and human activity data to explore the driving mechanism of the spatiotemporal variation in the YRB. Then, we will construct water area prediction and early warning models. Moreover, we will combine satellite altimetry data and high-precision terrain data to carry out dynamic monitoring of water storage in typical lakes and reservoirs in the YRB. Subsequently, we will provide detailed decision-supporting data for the planning, management, and servicing of water resources in the YRB.

6. Conclusions

Aiming to address the problems of a large concentration and spatiotemporal heterogeneity of SPM in surface water in the YRB, this study proposes the SWE-CSPM, which is based on the concept of classification and grading and considers the SPM concentration. Compared with nine typical water indexes and the MIWER, the SWE-CSPM significantly reduces the commission error, and the extraction accuracy is the highest (overall accuracy 95.44%, kappa coefficient 90.62%). This study examines the dynamic variations in the water area in the YRB from 1991 to 2023 at the global scale, the secondary water resource zoning scale, the provincial scale, and the typical water scale. This study finds that at the global scale, the area of maximum water shows a fluctuating downtrend, although the change range is small. The permanent water area shows an uptrend, whereas the seasonal water area shows a downtrend year by year. At the secondary water resource zoning scale, the permanent water area increases to varying degrees, except that the Interior Drainage Area remains stable. Among zonings, the zoning of Above Longyangxia experiences the most significant increase in the permanent water area. At the provincial scale, the permanent water area of each province has shown an uptrend, while the seasonal water area has shown a fluctuating downtrend. Only the maximum water area in Shandong Province, Inner Mongolia Autonomous Region, and Qinghai Province increases slowly, while the rest of the provinces show a downtrend. At the water bodies scale, the water area changes in Zhaling Lake, Eling Lake, Wuliangsuhai, Hongjiannao, and Dongping Lake are quite different. However, the permanent water area and maximum water area of the above water bodies have increased in the past decade, and the seasonal water area changes are small. Based on the above research results, we will further carry out surface water classification in the YRB and combine meteorological data and human activity data to explore the driving mechanism of the spatiotemporal variation in the YRB. Then, we will construct water area prediction and early warning models. Moreover, we will combine satellite altimetry data and high-precision terrain data to carry out dynamic monitoring of water storage in typical lakes and reservoirs in the YRB. Subsequently, we will provide detailed decision-supporting data for the planning, management, and servicing of water resources in the YRB.

Author Contributions: Overall design, Z.Z.; methodology, X.G. and Z.Z.; software, X.G. and Y.F.; formal analysis, L.C. and X.L.; writing—original draft preparation, Z.Z. and X.G.; writing—review and editing, X.Z., L.Y., H.Z. and X.X.; funding acquisition, L.C. All authors have read and agreed to the published version of the manuscript.

Funding: This research was funded by the National Key Research and Development Program of China (2022YFC3201703), the Open Fund of Key Laboratory of Geospatial Technology for the Middle and Lower Yellow River Regions (Henan University), Ministry of Education (GTYR202106), North

China University of Water Resources and Electric Power New Era Water Control Social Science Research Institute "Open list" project (24JB-01-02), Henan Province's 2023 Water Conservancy Science and Technology Research Project (GG202338), the Henan Province science and technology research and development plan joint fund project (232103810102), the Research Fund project of Key Laboratory of Water Management and Water Security in Yellow River Basin, Ministry of Water Resources (2023-SYSJJ-04), and the National Natural Science Foundation of China (42007423; 42201097).

Data Availability Statement: The data that support the findings of this study are available on request from the corresponding author. The data are not publicly available due to privacy restrictions. The data will be used for further exploration and analysis.

Acknowledgments: We would like to express our respect and gratitude to the anonymous reviewers and editors for their professional comments and suggestions.

Conflicts of Interest: The authors declare no conflicts of interest.

Appendix A

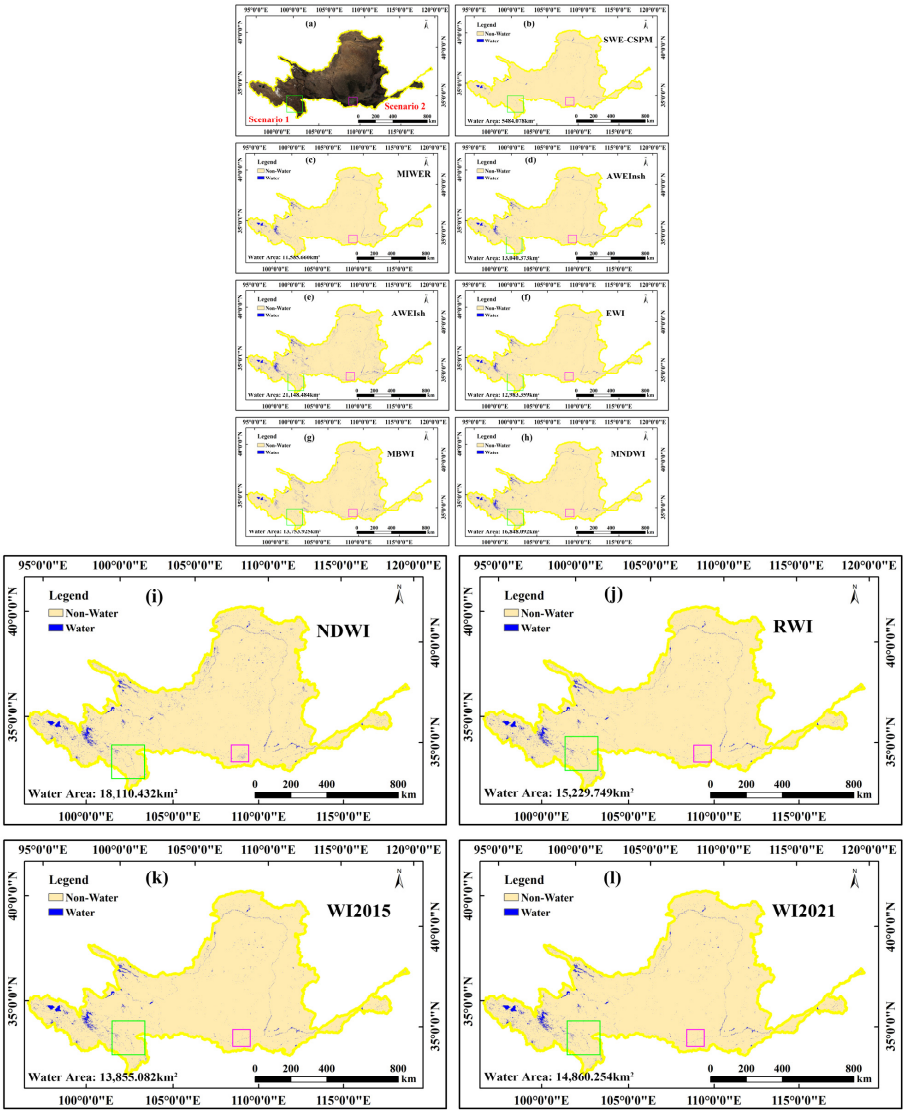

Figure A1. Surface water extraction based on 2021 synthetic images using various methods. Scenario 1 and scenario 2 are the high mountainous regions and urban regions, respectively. The green square in the figure represents scenario 1, and the purple square represents scenario 2. (**a**) Landsat 8 true colour images of the area. (**b**–**l**), respectively the extraction effect of SWE-CSPM MIWER, AWEInsh, AWEIsh, EWI, MBWI, MNDWI, NDWI, RWI, WI2015 and WI2021.

References

1. Yue, L.; Li, B.; Zhu, S.; Yuan, Q.; Shen, H. A fully automatic and high-accuracy surface water mapping framework on google earth engine using landsat time-series. *Int. J. Digit. Earth* **2023**, *16*, 210–233. [CrossRef]
2. Yamazaki, D.; Trigg, M.A. The dynamics of earth's surface water. *Nature* **2016**, *540*, 348–349. [CrossRef]
3. Zhang, Y.; Du, J.; Guo, L.; Fang, S.; Zhang, J.; Sun, B.; Mao, J.; Sheng, Z.; Li, L. Long-term detection and spatiotemporal variation analysis of open-surface water bodies in the Yellow River Basin from 1986 to 2020. *Sci. Total Environ.* **2022**, *845*, 157152. [CrossRef]
4. Cooley, S.W.; Ryan, J.C.; Smith, L.C. Human alteration of global surface water storage variability. *Nature* **2021**, *591*, 78–81. [CrossRef] [PubMed]
5. Scanlon, B.R.; Fakhreddine, S.; Rateb, A.; de Graaf, I.; Famiglietti, J.; Gleeson, T.; Grafton, R.Q.; Jobbagy, E.; Kebede, S.; Kolusu, S.R.; et al. Global water resources and the role of groundwater in a resilient water future. *Nat. Rev. Earth Environ.* **2023**, *4*, 87–101. [CrossRef]
6. Sogno, P.; Klein, I.; Kuenzer, C. Remote sensing of surface water dynamics in the context of global change—A review. *Remote Sens.* **2022**, *14*, 2475. [CrossRef]
7. Tulbure, M.G.; Broich, M.; Stehman, S.V.; Kommareddy, A. Surface water extent dynamics from three decades of seasonally continuous landsat time series at subcontinental scale in a semi-arid region. *Remote Sens. Environ.* **2016**, *178*, 142–157. [CrossRef]
8. Wang, X.; Xiao, X.; Zou, Z.; Dong, J.; Qin, Y.; Doughty, R.B.; Menarguez, M.A.; Chen, B.; Wang, J.; Ye, H.; et al. Gainers and losers of surface and terrestrial water resources in China during 1989–2016. *Nat. Commun.* **2020**, *11*, 3471. [CrossRef]
9. Guo, J.; Wang, X.; Liu, B.; Liu, K.; Zhang, Y.; Wang, C. Remote-Sensing Extraction of Small Water Bodies on the Loess Plateau. *Water* **2023**, *15*, 866. [CrossRef]
10. McFeeters, S.K. The use of the normalized difference water index (NDWI) in the delineation of open water features. *Int. J. Remote Sens.* **1996**, *17*, 1425–1432. [CrossRef]
11. Fisher, A.; Flood, N.; Danaher, T. Comparing landsat water index methods for automated water classification in eastern australia. *Remote Sens. Environ.* **2016**, *175*, 167–182. [CrossRef]
12. Xu, H. Modification of normalised difference water index (NDWI) to enhance open water features in remotely sensed imagery. *Int. J. Remote Sens.* **2006**, *27*, 3025–3033. [CrossRef]
13. Wang, S.; Baig, M.H.A.; Zhang, L.; Jiang, H.; Ji, Y.; Zhao, H.; Tian, J. A simple enhanced water index (EWI) for percent surface water estimation using landsat data. *IEEE J. Sel. Top. Appl. Earth Obs. Remote Sens.* **2015**, *8*, 90–97. [CrossRef]
14. Feyisa, G.L.; Meilby, H.; Fensholt, R.; Proud, S.R. Automated water extraction index: A new technique for surface water mapping using landsat imagery. *Remote Sens. Environ.* **2014**, *140*, 23–35. [CrossRef]
15. Wang, X.; Xie, S.; Zhang, X.; Chen, C.; Guo, H.; Du, J.; Duan, Z. A robust multi-band water index (MBWI) for automated extraction of surface water from landsat 8 OLI imagery. *Int. J. Appl. Earth Obs. Geoinf.* **2018**, *68*, 73–91. [CrossRef]
16. Hu, R.; Yao, Z.; LI, P.; Sun, Y.; Jia, Y. Construction and stability study of water index of Landsat-8 images. *Sci. Surv. Mapp.* **2022**, *47*, 150–155. [CrossRef]
17. Wu, Q.; Wang, M.; Shen, X.; Yao, Y.; Li, J.; Zhang, F.; Zhou, Y. Small water body extraction method based on Sentinel-2 satellite multi-spectral remote sensing image. *Natl. Remote Sens. Bull.* **2022**, *26*, 781–794. [CrossRef]
18. Zhang, D.-D.; Xu, J. Long-Term Monitoring of Surface Water Dynamics and Analysis of Its Driving Mechanism: A Case Study of the Yangtze River Basin. *Water* **2024**, *16*, 677. [CrossRef]
19. Zou, Z.; Xiao, X.; Dong, J.; Qin, Y.; Doughty, R.B.; Menarguez, M.A.; Zhang, G.; Wang, J. Divergent trends of open-surface water body area in the contiguous United States from 1984 to 2016. *Proc. Natl. Acad. Sci. USA* **2018**, *115*, 3810–3815. [CrossRef]
20. Xie, G.; Bai, X.; Peng, Y.; Li, Y.; Zhang, C.; Liu, Y.; Liang, J.; Fang, L.; Chen, J.; Men, J.; et al. Aquaculture ponds identification based on multi-feature combination strategy and machine learning from landsat-5/8 in a typical inland lake of China. *Remote Sens.* **2024**, *16*, 2168. [CrossRef]
21. Hibjur Rahaman, M.; Roshani; Masroor, M.; Sajjad, H. Integrating remote sensing derived indices and machine learning algorithms for precise extraction of small surface water bodies in the lower *thoubal* river watershed, India. *J. Clean. Prod.* **2023**, *422*, 138563. [CrossRef]
22. Si, Y.; Gong, D.; Guo, Y.; Zhu, X.; Huang, Q.; Evans, J.; He, S.; Sun, Y. An advanced spectral–spatial classification framework for hyperspectral imagery based on DeepLab v3+. *Appl. Sci.* **2021**, *11*, 5703. [CrossRef]
23. Qi, Z.; Wang, B.; Tian, Y.; Zhang, P. When ensemble learning meets deep learning: A new deep support vector machine for classification. *Knowl. Based Syst.* **2016**, *107*, 54–60. [CrossRef]
24. Li, Y.; Dang, B.; Zhang, Y.; Du, Z. Water body classification from high-resolution optical remote sensing imagery: Achievements and perspectives. *ISPRS J. Photogramm. Remote Sens.* **2022**, *187*, 306–327. [CrossRef]
25. Wangchuk, S.; Bolch, T. Mapping of glacial lakes using sentinel-1 and sentinel-2 data and a random forest classifier: Strengths and challenges. *Sci. Remote Sens.* **2020**, *2*, 100008. [CrossRef]
26. Li, J.; Ma, R.; Cao, Z.; Xue, K.; Xiong, J.; Hu, M.; Feng, X. Satellite Detection of Surface Water Extent: A Review of Methodology. *Water* **2022**, *14*, 1148. [CrossRef]
27. Xu, Y.; Lin, J.; Zhao, J.; Zhu, X. New method improves extraction accuracy of lake water bodies in central asia. *J. Hydrol.* **2021**, *603*, 127180. [CrossRef]
28. Irvin, B.J.; Ventura, S.J.; Slater, B.K. Fuzzy and isodata classification of landform elements from digital terrain data in pleasant valley, wisconsin. *Geoderma* **1997**, *77*, 137–154. [CrossRef]

29. Liu, Z. Identifying urban land use social functional units: A case study using OSM data. *Int. J. Digit. Earth* **2021**, *14*, 1798–1817. [CrossRef]
30. Xing, H.; Niu, J.; Feng, Y.; Hou, D.; Wang, Y.; Wang, Z. A coastal wetlands mapping approach of yellow river delta with a hierarchical classification and optimal feature selection framework. *Catena* **2023**, *223*, 106897. [CrossRef]
31. Mao, D.; Wang, Z.; Du, B.; Li, L.; Tian, Y.; Jia, M.; Zeng, Y.; Song, K.; Jiang, M.; Wang, Y. National wetland mapping in China: A new product resulting from object-based and hierarchical classification of landsat 8 OLI images. *ISPRS J. Photogramm. Remote Sens.* **2020**, *164*, 11–25. [CrossRef]
32. Jiang, W.; He, G.; Long, T.; Ni, Y.; Liu, H.; Peng, Y.; Lv, K.; Wang, G. Multilayer perceptron neural network for surface water extraction in landsat 8 OLI satellite images. *Remote Sens.* **2018**, *10*, 755. [CrossRef]
33. Zhang, Z.; Zhang, X.; Jiang, X.; Xin, Q.; Ao, Z.; Zuo, Q.; Chen, L. Automated surface water extraction combining sentinel-2 imagery and OpenStreetMap using presence and background learning (PBL) algorithm. *IEEE J. Sel. Top. Appl. Earth Obs. Remote Sens.* **2019**, *12*, 3784–3798. [CrossRef]
34. Li, K.; Wang, J.; Cheng, W.; Wang, Y.; Altansukh, O. Deep learning empowers the google earth engine for automated water extraction in the lake baikal basin. *Int. J. Appl. Earth Obs. Geoinf.* **2022**, *112*, 102928. [CrossRef]
35. Li, K.; Wang, J.; Yao, J. Effectiveness of machine learning methods for water segmentation with ROI as the label: A case study of the tuul river in Mongolia. *Int. J. Appl. Earth Obs. Geoinf.* **2021**, *103*, 102497. [CrossRef]
36. Li, L.; Yan, Z.; Shen, Q.; Cheng, G.; Gao, L.; Zhang, B. Water body extraction from very high spatial resolution remote sensing data based on fully convolutional networks. *Remote Sens.* **2019**, *11*, 1162. [CrossRef]
37. Fu, G.; Liu, C.; Zhou, R.; Sun, T.; Zhang, Q. Classification for High Resolution Remote Sensing Imagery Using a Fully Convolutional Network. *Remote Sens.* **2017**, *9*, 498. [CrossRef]
38. Li, Z.; Zhang, X.; Xiao, P. Spectral index-driven FCN model training for water extraction from multispectral imagery. *ISPRS J. Photogramm. Remote Sens.* **2022**, *192*, 344–360. [CrossRef]
39. Cao, H.; Tian, Y.; Liu, Y.; Wang, R. Water body extraction from high spatial resolution remote sensing images based on enhanced U-Net and multi-scale information fusion. *Sci. Rep.* **2024**, *14*, 16132. [CrossRef]
40. Sun, D.; Gao, G.; Huang, L.; Liu, Y.; Liu, D. Extraction of water bodies from high-resolution remote sensing imagery based on a deep semantic segmentation network. *Sci. Rep.* **2024**, *14*, 14604. [CrossRef]
41. Chen, L.-C.; Papandreou, G.; Kokkinos, I.; Murphy, K.; Yuille, A.L. DeepLab: Semantic image segmentation with deep convolutional nets, atrous convolution, and fully connected CRFs. *arXiv* **2017**, arXiv:1606.00915. [CrossRef]
42. Tao, Y.; Xu, M.; Zhong, Y.; Cheng, Y. GAN-assisted two-stream neural network for high-resolution remote sensing image classification. *Remote Sens.* **2017**, *9*, 1328. [CrossRef]
43. Chang, L.-C.; Wang, W.-H.; Chang, F.-J. Explore training self-organizing map methods for clustering high-dimensional flood inundation maps. *J. Hydrol.* **2021**, *595*, 125655. [CrossRef]
44. Yuan, Q.; Shen, H.; Li, T.; Li, Z.; Li, S.; Jiang, Y.; Xu, H.; Tan, W.; Yang, Q.; Wang, J.; et al. Deep learning in environmental remote sensing: Achievements and challenges. *Remote Sens. Environ.* **2020**, *241*, 111716. [CrossRef]
45. Cheng, G.; Xie, X.; Han, J.; Guo, L.; Xia, G.-S. Remote sensing image scene classification meets deep learning: Challenges, methods, benchmarks, and opportunities. *IEEE J. Sel. Top. Appl. Earth Obs. Remote Sens.* **2020**, *13*, 3735–3756. [CrossRef]
46. Sekertekin, A. A survey on global thresholding methods for mapping open water body using sentinel-2 satellite imagery and normalized difference water index. *Arch. Comput. Methods Eng.* **2021**, *28*, 1335–1347. [CrossRef]
47. Liu, Z.; Cui, T.; Zhang, S.; Zhao, W. Landsat8 OLI piecewise linear inversion of suspended matter concentration in the Yellow River Estuary. *Spectrosc. Spectr. Anal.* **2018**, *38*, 2536–2541. [CrossRef]
48. Yang, Y.; Lü, Y.; Fu, B.; Wu, X.; Wang, S.; Wu, T. The potential for carbon sequestration by afforestation can be limited in dryland river basins under the pressure of high human activity. *Sci. Total Environ.* **2023**, *858*, 159817. [CrossRef]
49. Mehta, P.; Siebert, S.; Kummu, M.; Deng, Q.; Ali, T.; Marston, L.; Xie, W.; Davis, K.F. Half of twenty-first century global irrigation expansion has been in water-stressed regions. *Nat. Water* **2024**, *2*, 254–261. [CrossRef]
50. Qu, L.; Lei, T.; Ning, D.; Civco, D.; Yang, X. A spectral mixing algorithm for quantifying suspended sediment concentration in the yellow river: A simulation based on a controlled laboratory experiment. *Int. J. Remote Sens.* **2016**, *37*, 2560–2584. [CrossRef]
51. Zhao, Z.; Li, H.; Song, X.; Sun, W. Dynamic monitoring of surface water bodies and their influencing factors in the yellow river basin. *Remote Sens.* **2023**, *15*, 5157. [CrossRef]
52. Cao, H.; Han, L.; Li, L. Changes in extent of open-surface water bodies in China's Yellow River Basin (2000–2020) using Google Earth Engine cloud platform. *Anthropocene* **2022**, *39*, 100346. [CrossRef]
53. Jiang, L.; Liu, Y. Response of Runoff-Sediment System to Vegetation Variation in the Yellow River Basin in the Last 20 Years. *Land* **2023**, *12*, 428. [CrossRef]
54. Li, P.; Ke, Y.; Wang, D.; Ji, H.; Chen, S.; Chen, M.; Lyu, M.; Zhou, D. Human impact on suspended particulate matter in the Yellow River Estuary, China: Evidence from remote sensing data fusion using an improved spatiotemporal fusion method. *Sci. Total Environ.* **2021**, *750*, 141612. [CrossRef] [PubMed]
55. Hu, Q.; Li, C.; Wang, Z.; Liu, Y.; Liu, W. Continuous Monitoring of the Surface Water Area in the Yellow River Basin during 1986–2019 Using Available Landsat Imagery and the Google Earth Engine. *ISPRS Int. J. Geo-Inf.* **2022**, *11*, 305. [CrossRef]
56. Deng, Y.; Jiang, W.; Tang, Z.; Ling, Z.; Wu, Z. Long-Term Changes of Open-Surface Water Bodies in the Yangtze River Basin Based on the Google Earth Engine Cloud Platform. *Remote Sens.* **2019**, *11*, 2213. [CrossRef]

57. Li, Z.; Xu, Y.; Sun, Y.; Wu, M.; Zhao, B. Urbanization-driven changes in land-climate dynamics: A case study of haihe river basin, China. *Remote Sens.* **2020**, *12*, 2701. [CrossRef]
58. Jia, X.; Jin, Z.; Mei, X.; Wang, D.; Zhu, R.; Zhang, X.; Huang, Z.; Li, C.; Zhang, X. Monitoring and effect evaluation of an ecological restoration project using multi-source remote sensing: A case study of wuliangsuhai watershed in China. *Land* **2023**, *12*, 349. [CrossRef]
59. Jing, W.; Yao, L.; Zhao, X.; Zhang, P.; Liu, Y.; Xia, X.; Song, J.; Yang, J.; Li, Y.; Zhou, C. Understanding Terrestrial Water Storage Declining Trends in the Yellow River Basin. *J. Geophys. Res. Atmos.* **2019**, *124*, 12963–12984. [CrossRef]
60. Lin, M.; Biswas, A.; Bennett, E.M. Spatio-temporal dynamics of groundwater storage changes in the Yellow River Basin. *J. Environ. Manag.* **2019**, *235*, 84–95. [CrossRef]